

UCSF

UC San Francisco Electronic Theses and Dissertations

Title

Investigating the role of the dynamic chromatin landscape in hippocampal-dependent cognitive function

Permalink

<https://escholarship.org/uc/item/1gp0g8hb>

Author

Pratt, Karishma

Publication Date

2023

Peer reviewed|Thesis/dissertation

Investigating the Role of the Dynamic Chromatin Landscape in Hippocampal-dependent Cognitive Function

by
Karishma Pratt

THESIS

Submitted in partial satisfaction of the requirements for degree of
DOCTOR OF PHILOSOPHY

in

Developmental and Stem Cell Biology

in the

GRADUATE DIVISION

of the

UNIVERSITY OF CALIFORNIA, SAN FRANCISCO

Approved:

DocuSigned by:

Daniel Lim

Daniel Lim

FC7A2B6D45EF428...

Chair

DocuSigned by:

Barbara Panning

Barbara Panning

DocuSigned by:

Dena Dubal

Dena Dubal

DocuSigned by:

Saul Villeda

Saul Villeda

711626DA5837464...

Committee Members

Copyright 2023

by

Karishma Pratt

Acknowledgements

First and foremost, I would like to thank my mentor, Saul Villeda, for instilling confidence in me and teaching me how to think critically as a scientist. He is an exemplary leader who exudes attentiveness and understanding and deeply values the well-being of his lab members. During my time in his lab, he provided me with the necessary support and guidance when I needed it while also encouraging me to explore scientific pursuits independently as I advanced as a student. His unwavering dedication to our happiness and growth has allowed me to develop and thrive and I am extremely grateful for his mentorship at UCSF.

I would also like to express my immense gratitude to the other members of my thesis committee, Daniel Lim, Barbara Panning, and Dena Dubal, for their scientific expertise and support throughout the years. Barbara and Dena both served on my qualifying exam committee, and Daniel Lim served as my thesis committee chair. It has been an honor to learn from a group of such brilliant and helpful scientists, and I am grateful to have had their guidance through the years.

I have been incredibly fortunate to have worked in such an amazing environment, with people that have become my closest friends. I sincerely thank the members of the Villeda lab for always helping me, for providing their own insights and expertise, for getting coffee with me almost daily, and for making the time we spent together so memorable both in and outside of lab. I thank my friends in my graduate program for being such a wonderful group of people, with a special shoutout to my cohort and the good friends I've made. From Yosemite to Tahoe to Pagan Idol to late-night reagent swapping, we've made priceless memories together. They are a selfless and amazing group of people, always trying to help their fellow peer. There are so many inspirational students, postdocs and other faculty that I have met during my time in San Francisco, and I am grateful to have learned from every single one of them.

Most of all, I would like to thank my family. I thank my grandmother, the first PhD in the family, for always supporting me and showering me with love. I thank my wonderful friends who I cherish deeply as the family I have chosen. I thank all my extended family, including my cousins, aunts and uncles, for providing inspiration and support. I thank my brother, sister, mother and father-in-law for their utmost love and guidance during this whole process. I thank my husband, Anish, for being the most supportive human a person could ask for and for helping me through this entire program. Lastly, I thank my parents for their unwavering love and ample encouragement and support. I would not have been able to accomplish any of this without the love and dedication of my family. Thank you for listening to me talk about science for the last six years. I love you all so much.

Investigating the role of the dynamic chromatin landscape in hippocampal-dependent cognitive function

Karishma Pratt

ABSTRACT

At present, there are no means to counter functional loss in the aging brain underlying both normal cognitive decline and neurodegenerative disease in the elderly. As such, defining key regulatory molecular signatures associated with age-related functional decline may help identify potential targets to restore cognition at old age. To define the temporal kinetics of age-related cognitive decline, we first assessed several modalities of hippocampal-dependent learning and memory in the mouse species at young (3 months), mature (6 months), middle-aged (12 months), aged (18 months) and old (24 months) ages. We observed that the rate of cognitive decline was indeed different across distinct types of learning and memory, with recognition and associative memory impairments occurring at faster kinetics compared to spatial and working memory deficits. To define molecular changes associated with age-related cognitive decline, we performed single nucleus RNA sequencing (snRNA seq) and chromatin accessibility sequencing (snATAC-seq) on hippocampi from young and aged mice. We characterized differences in cell-type specific gene expression patterns and DNA regulatory elements during aging. We then delved deeper into another critical mechanism of DNA regulation, DNA methylation, which has emerged as a critical modulator of neuronal plasticity and cognitive function. Notwithstanding, the role of enzymes that demethylate DNA, the Ten-Eleven Translocation (TET1-3) enzymes, remains to be fully explored. In the adult mouse hippocampus, we detected an enrichment of Tet2 in neurons. Viral-mediated neuronal overexpression and RNA interference of Tet2 altered dendritic complexity and synaptic-plasticity-related gene expression in vitro. Overexpression of neuronal Tet2 in adult hippocampus, and loss of Tet2 in adult glutamatergic neurons, resulted in differential hydroxymethylation

associated with genes involved in synaptic transmission. Functionally, overexpression of neuronal Tet2 impaired hippocampal-dependent memory, while loss of neuronal Tet2 enhanced memory. These data identify neuronal Tet2 as a molecular target to boost cognitive function. Overall, this work has significant translational potential by identifying underlying chromatin and molecular mechanisms in cognitive function.

Table of Contents

Chapter 1. Defining temporal heterogeneity and molecular mechanisms of age-related cognitive impairment across the mouse lifespan.....	1
Materials and methods	24
References	27
Chapter 2. Loss of neuronal Tet2 enhances hippocampal dependent cognitive function.....	30
Materials and methods	62
References.....	73

LIST OF FIGURES

Chapter 1

Figure 1. Cognitive decline is temporally heterogeneous in in the mouse model, both between different cognitive modalities and between subjects	7
Figure 2. Cognitive decline is temporally heterogeneous in in the mouse model, both between different cognitive modalities and between subjects.....	10
Figure 3. Z-score analysis of hippocampal-dependent cognitive function shows heterogeneous decline between subjects and cognitive modalities.....	12
Figure 4. Single nucleus RNA sequencing identifies transcriptional changes between young and aged hippocampi	15
Figure 5. Single nucleus ATAC sequencing from young and aged mice identifies shifts in oligodendrocyte and microglia subpopulations.....	17
Figure 6. Analysis of differentially accessible regions in aging oligodendrocytes and microglia	19
Figure 7. Single nucleus RNA sequencing of exercised mice identifies potential rejuvenation profile in the aging hippocampus.....	21

Chapter 2

Figure 1. Schematic representation of demethylation of cytosine.....	35
Figure 2. Tet2 transcript is enriched in neurons in the hippocampus.....	38
Figure 3. Tet2 alters neuronal morphology in vitro.....	40
Figure 4. Tet expression and cell viability in primary neurons following neuronal Tet2 overexpression and abrogation.....	41
Figure 5. Tet2 regulates synaptic-related gene expression <i>in vitro</i>	44
Figure 6. Increased neuronal Tet2 in the adult hippocampus alters hydroxymethylation on genes related to synaptic processes and impairs memory.....	48
Figure 7. Validation of neuronal nuclei isolation and overall health analysis following in vivo viral-mediated neuronal Tet2 overexpression.....	50
Figure 8. Tet2 loss in adult excitatory neurons alters hydroxymethylation on genes related to synapses and enhances hippocampal-dependent memory.....	53
Figure 9. Tet expression and overall health analysis following temporally controlled in vivo loss of neuronal Tet2.....	55
Figure 10. Graphical abstract of Chapter 2.....	59

Chapter 1

Defining temporal heterogeneity and molecular mechanisms of age-related cognitive impairment across the mouse lifespan

Karishma Pratt¹⁻² and Saul A. Villeda^{1-3*}

1. Department of Anatomy, University of California San Francisco, San Francisco, California 94143, USA
2. Developmental and Stem Cell Biology Graduate Program, University of California San Francisco, San Francisco, California 94143, USA
3. Bakar Aging Research Institute, San Francisco, California, 94143, USA

AUTHOR CONTRIBUTIONS:

K.P. and S.A.V. developed concept and designed experiments. K.P. performed *in vivo* and molecular studies. K.P. wrote this chapter. S.A.V supervised all aspects of the project.

ABSTRACT

At present, there are no means to counter functional loss in the aging brain underlying both normal cognitive decline and dementia-related neurodegenerative disease in the elderly. As such, defining key regulatory molecular signatures in the aging brain associated with functional decline may help identify potential targets to restore cognition at old age. Given onset of cognitive impairments is not uniform across cognitive modalities, we sought to delineate the ages at which individual learning and memory processes exhibit deterioration. To define the temporal kinetics of age-related cognitive decline, we first assessed hippocampal-dependent learning and memory in the mouse species across the lifespan using novel object recognition (recognition memory), radial arm water maze (spatial learning and memory), and Y-maze (working memory) at young (3 months), mature (6 months), middle-aged (12 months), aged (18 months) and old (24 months) ages. We observed that the rate of cognitive decline was indeed different across distinct types of learning and memory, with recognition and associative memory impairments occurring at faster kinetics compared to spatial and working memory deficits. Young mice outperformed all age groups in recognition and associative memory, while mice that were middle-aged performed comparable to younger groups in spatial memory and working memory tasks. To define molecular changes associated with age-related cognitive decline, we performed single nucleus RNA sequencing (snRNA seq) and single nucleus chromatin accessibility sequencing (snATAC-seq) on hippocampi from young and aged mice and characterized differences in cell-type specific gene expression patterns and DNA regulatory elements during aging. Finally, we investigated the mechanisms of brain rejuvenation in response to exercise by profiling the transcriptome and comparing to our aging dataset. Overall, this work has significant translational potential by identifying temporal heterogeneity of dysfunction and underlying molecular mechanisms in cognitive decline.

Introduction

Brain Aging and Cognitive Decline

Aging in the brain results in significant decline in cognitive function and increased susceptibility to devastating dementia-related neurodegenerative disorders such as Alzheimer's disease (AD) (Bieri et al., 2023). Given the rate at which the human population is aging, it is critical to identify key drivers and mechanisms of brain aging in order to prevent age-related cognitive decline and associated neurodegenerative diseases. Among the established hallmarks of aging, key cellular and molecular features that correspond with the aging phenotype across species and cell types, several are related to DNA integrity, including decreased genomic stability, disruption of chromatin organization, alterations in post-translational histone modifications, and shifts in DNA methylation (López-Otín et al., 2013).

Of particular interest within the brain is the hippocampus, the brain region responsible for multiple types of learning and memory and highly susceptible to aging (Fan et al., 2017). The hippocampus is comprised of a tri-synaptic circuit, where the Dentate Gyrus receives input from the entorhinal cortex and sends signal through mossy fibers to the CA3, CA2, and CA1 neurons. The hippocampus is comprised of numerous cell types, including microglia (immune cells), supporting cells such as astrocytes, myelinating oligodendrocytes, and specialized cell types around the blood brain barrier. With age, there is functional decline across cell types, including changes in neuronal circuitry and decreased synaptic plasticity, decreased regenerative capacity of progenitor cell types, increased microglia and astrocyte activation, and increased permeability of the blood brain barrier (Bieri et al., 2023).

Cognitive decline in humans with age is heterogeneous

Human studies have examined cognitive decline in various modalities, revealing that the degree and pace of deterioration varies widely among individuals (Nyberg et al., 2012). Cognitive decline does not follow a uniform pattern across either individuals or cognitive functions of the brain (Gonzales et al., 2022). The factors that underlie these individual differences in the trajectory of cognitive decline remain elusive.

Our lab, along with many others, utilizes the mouse species as a model of cognitive decline with age. The mouse species exhibits significant decline in learning and memory, particularly spatial learning and memory, and this has been correlated with changes in the hippocampus. We asked whether there is variability in cognitive decline in the mouse model, similar to humans, by assaying several cognitive functions across the mouse lifespan. By better understanding cognitive decline in mouse models, we can perhaps identify what molecular mechanisms drive this heterogeneity in humans.

Molecular mechanisms of brain aging

Several papers have recently been published beginning to look at changes in transcription in the hippocampus or with age (Allen et al., 2023; Morabito et al., 2021; Ximerakis et al., 2019). However, significant questions remain in the field. While groups have characterized transcriptional changes, we have yet to link molecular mechanisms to functional decline in cognitive ability. Similarly, we have yet to look at the underlying chromatin landscape in young and aged mice. To answer this question, we will perform cognitive testing across the mouse lifespan and subsequently perform single nucleus RNA and ATAC sequencing, allowing us to correlate gene signatures, chromatin signatures, and cognitive ability.

In this study, we have performed an aging timecourse and assessed cognition in mice at 3,6,12,18, and 24 months of age. We then performed snRNA-seq and snATAC seq on separate

cohorts of young and aged mice and observed marked differences in cell-type specific gene expression patterns and DNA regulatory elements during aging in the hippocampus. Finally, we compared transcription in the hippocampus between young, aged, and aged exercised mice, a known rejuvenation paradigm (Horowitz et al., 2020). Together, this data will pinpoint key regulatory domains in cognitive decline associated with healthy aging.

RESULTS

Characterizing the cognitive trajectory of aging mice.

To appreciate the heterogeneity of cognitive decline in the mouse model, we performed several behavioral assays across the mouse lifespan. We tested C57/Bl6 male mice at 3 months, 6 months, 12 months, 18 months, and 24 months of age in a cross-sectional study (Figure 1A). We first assessed movement and anxiety in an open field test (OFT), where mice are allowed to explore a plain chamber for 10 minutes. We found that the total distance traveled during testing declined by 18 months of age (Figure 1B). We assessed anxiety by measuring the amount of time spent in the center of the arena versus the perimeter or corners and observed no difference between ages in this specific cohort (Figure 1C). We next tested Novel Object Recognition memory, in which two identical objects are placed in the same open field arena. On day 1, mice are allowed to explore the arena including the objects for five minutes. On day 2, one object is swapped for a novel object, and mice are then allowed to explore the arena for five minutes. Mice will spend more time with the novel object if they remember the familiar object. We find that this discrimination declines by 18 months of age (Figure 1D).

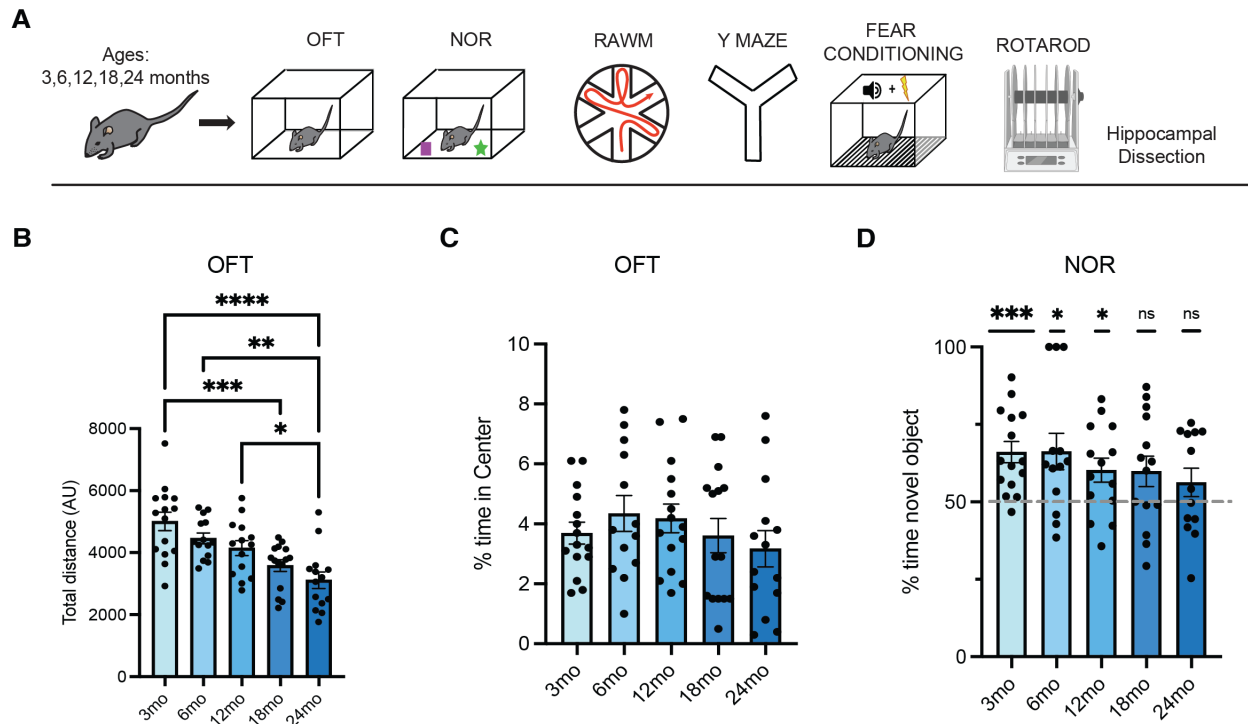


Figure 1. Cognitive decline is temporally heterogeneous in the mouse model, both between different cognitive modalities and between subjects.

A, Schematic illustrating the timeline of behavior paradigms for mice ages 3 months (n=15), 6 months (n=14), 12 months (n=14), 18 months (n=15) and 24 months (n=14).

B, Movement was assessed by Open Field Testing (OFT), where mice explore a plain chamber for a total of 10 minutes.

C, Anxiety was measured by time spent in the center of Open Field Testing (OFT), where mice explore a plain chamber for a total of 10 minutes.

D, Object recognition memory was assessed by Novel Object Recognition (NOR), as time spent exploring a novel object relative to a familiar object, 24 h after training. Data is shown as percent time spent with novel object between the two objects and compared against 50%, or equal time with each object.

Data shown as mean \pm SEM; *p<0.05, **p<0.01, ***p<0.001; (B,C) One Way ANOVA; (D) one-sample t-test vs 50%.

Spatial learning and memory declines with age

We next performed Radial Arm Water Maze to test spatial learning and memory. Mice learn to find a platform in an eight arm pool with spatial cues during 12 trials on Day 1 (3 trials per block), are tested 1 hour later on Day 1 to assess short-term memory, and then tested for fifteen more trials on Day 2 to assess long-term memory. We found that mice at ages 3, 6, and 12 months of age performed indistinguishably from one another during both training and testing (Figure 2A, 2B). By 18 months of age, however, young mice made significantly fewer errors during the training phase and when testing short term memory (Figure 2E). On Day 2, 18 month old mice trended toward making more errors ($p = 0.1$) than young mice (Figure 2C). By 24 months of age, aged mice made significantly more errors in both Block 5 and over the course of Day 2, indicating impairments in spatial short and long-term memory compared to 3 month old mice (Figure 2D, 2E).

Working memory declines by 24 months of age

We tested working memory by using the Forced Alternation Y-maze paradigm. Mice are trained on one arm in a Y-shaped maze, and 30 minutes after, a novel third arm is opened. Mice should demonstrate a preference toward the novel arm due to their innate curiosity. When assessing the discrimination index between novel and trained arms, we saw that mice spent more time in the novel over trained arm at 3, 6, 12, and 18 months of age. By 24 months of age, mice no longer spent significantly more time in the novel arm, indicating a decline in working spatial memory (Figure 2F). However, the mean of the discrimination indices at 24 months of age was above zero, indicating a slight preference for the novel arm. This type of memory is perhaps preserved well throughout life.

Motor coordination declines by 18 months of age

Lastly, we tested motor coordination and learning with the rotarod paradigm, where we train mice on a rotating platform and test over three trials 24 hours after training. By measuring the latency to fall off the rotating platform, we observed a significant decline in motor coordination by 18 months of age (Figure 2G). In conclusion, we find that the rate of cognitive decline is heterogeneous between different cognitive modalities.

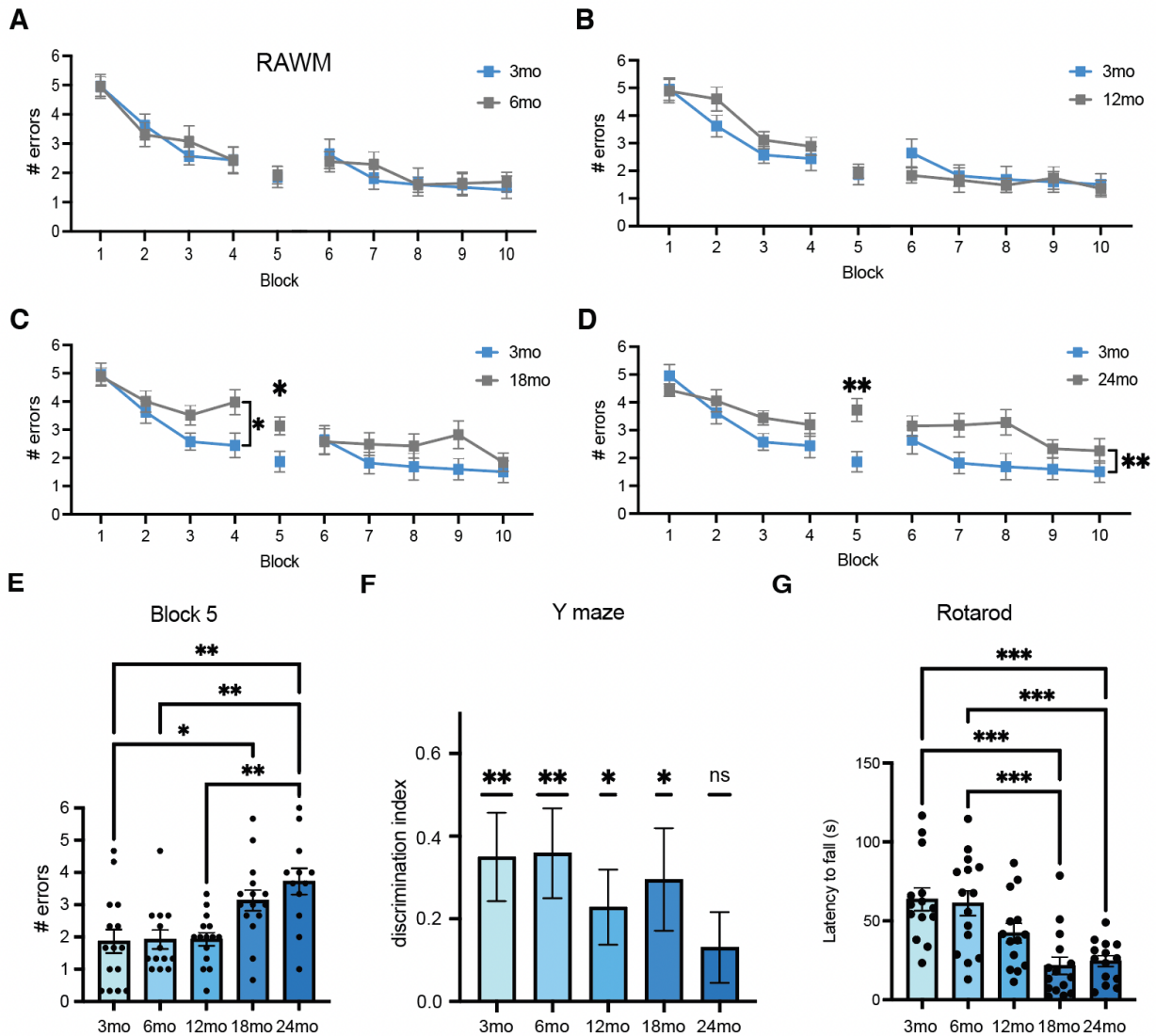


Figure 2. Cognitive decline is temporally heterogeneous in the mouse model, both between different cognitive modalities and between subjects.

A-D, Spatial learning and memory was assessed by Radial Arm Water Maze (RAWM), as number of errors made until finding the platform in an 8-arm water maze over two days (Day 1 Training: Blocks 1-4, Day 1 Short-term memory testing: Block 5, Day 2 Long-term memory testing: Blocks 6-10).

E, Comparison of Block 5 from RAWM testing short term spatial memory.

F, Working memory was assessed by Forced Alternation Y-maze. Discrimination index is shown as preference for novel arm over trained arm by percent time in one minute of testing. Zero is no preference for either arm.

G, Motor coordination was measured by Rotarod testing, where latency (seconds) to fall off a rotating axis over three trials on day 2 is shown.

Data shown as mean \pm SEM; * p <0.05, ** p <0.01, *** p <0.001; (A-D) ANOVA with Turkey's post-hoc test for multiple comparisons; (E,G) One Way ANOVA (F) one-sample t-test vs zero.

Cognitive decline is heterogeneous within subjects.

To determine whether cognitive decline was consistent across different modalities per subject, we used a Z-score analysis of cognitive performance followed by hierarchical clustering. We found that, while generally mice clustered by age, cognitive decline was indeed heterogeneous. Certain aged mice only exhibited cognitive decline in certain tasks, while some exhibited cognitive decline across all modalities. Notably, some aged mice exhibited cognitive resilience, clearly clustering with young mice and performing well across several cognitive modalities (Figure 3).

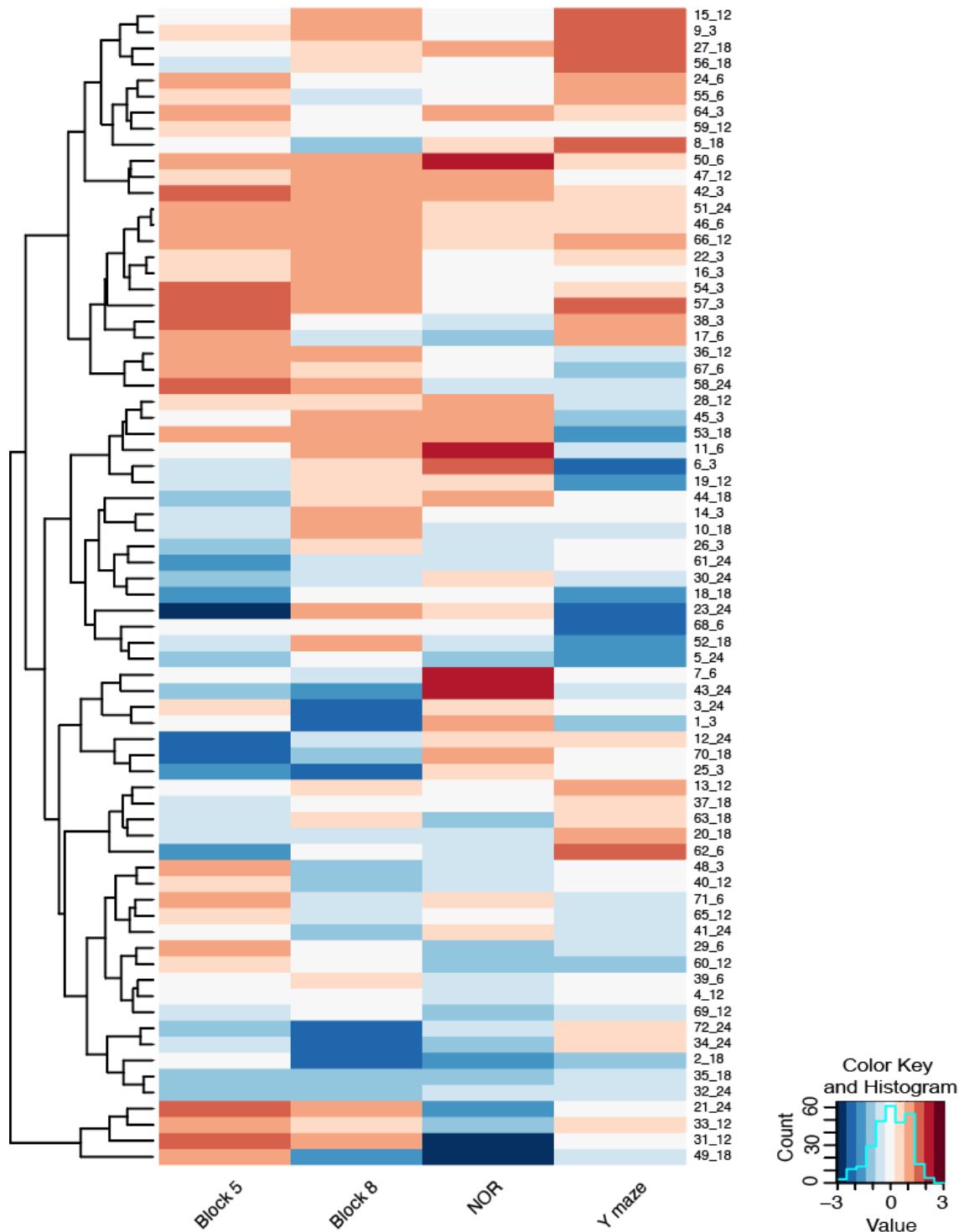


Figure 3. Z-score analysis of hippocampal-dependent cognitive function shows heterogeneous decline between subjects and cognitive modalities. Heatmap with hierarchical clustering of Z-scores of cognitive performances across 72 mice at ages 3,6,12,18 and 24 months of age. Subjects are labeled as “Subject Number_Age in months”. Analysis of RAWM values at Block 5, Block 8, percent time with novel object in NOR, and discrimination index in Y maze. Color Key and Histogram of heatmap on the right.

Single nucleus RNA sequencing of the aging mouse hippocampus

To start investigating molecular mechanisms linked to age-related cognitive decline, we first surveyed the hippocampi of young and aged male mice by single nucleus RNA sequencing (snRNA-seq) (n = 2 per age) (Figure 4A). After normalizing and filtering the data, the dataset contained 27,928 nuclei. Dimensional reduction and k-means clustering was visualized by UMAP projection and we were able to identify 25 distinct cell type clusters (Figure 4B). We matched clusters to known cell types by examining expression of cell-type specific genes and other publicly available datasets (**Zalocusky et al., 2021**) (Figure 4B). By utilizing single-nucleus over single-cell technology, we were able to retain significantly more neuronal nuclei, identify different neurons of the trisynaptic circuit, and deeply sequence neuronal populations.

SnRNA-seq identifies transcriptional changes across multiple cell types

After identifying cell type clusters, we ran differential gene expression between young and aged clusters using Seurat pipelines (Satija et al., 2015). Interestingly, we found that the most differential gene expression between young and aged hippocampi was in oligodendrocytes, followed by the neurons of the dentate gyrus (Figure 4C). We put the list of differential gene expression for aging oligodendrocytes through Gene Ontology analysis of biological processes and found changes in processes related to axon development and synapse organization (Figure 4D). As proof that we are capturing biologically relevant data, we also checked differential gene expression in microglia. Microglia become more activated with age (Bieri et al., 2023), and their functional changes have been shown to play roles in neurodegenerative diseases such as AD (Deczkowska et al., 2018). Indeed, we show that genes that increase expression in microglia with age are related to biological processes such as cell activation and immune response (Figure 4E). When we survey known activated microglia markers, we observe an increase in gene expression

of inflammatory markers with age (Figure 4F). Overall, this data demonstrates that several important transcriptional changes occur across different hippocampal cell types with age, with oligodendrocytes showing marked changes in transcriptional output. Lastly, while we found cell-type specific changes in transcriptional output, we also found signaling pathways that were globally downregulated in all cell types, particularly Robo/Slit signaling (Figure 4G). Understanding global and cell type specific transcriptional regulation will be important for further therapeutic development and research of the aging brain.

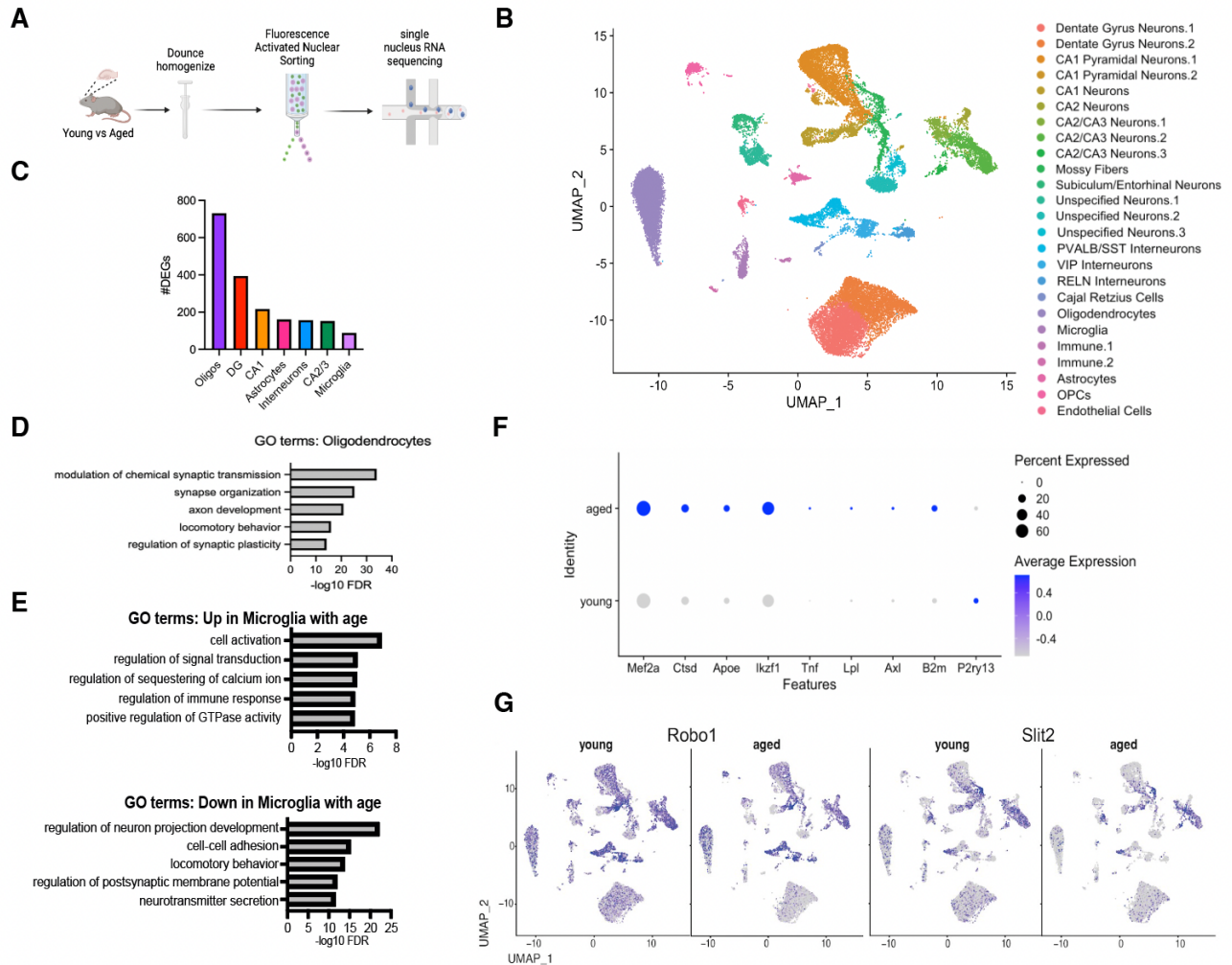


Figure 4. snRNA sequencing identifies transcriptional changes between young and aged hippocampi.

A, Schematic illustrating the paradigm for single nucleus RNA sequencing from hippocampi dissected from young (3 month old) and aged (22 month old) mice.

B, UMAP projection of 27,928 cells labeled by cell type

C, Bar graph of differentially expressed genes per cluster

D, Top significant gene ontology terms derived from differential gene expression lists between young and aged oligodendrocytes

E, Top significant gene ontology terms derived from differential gene expression lists between young and aged microglia

F, Dot plot of several known activation genes between young and aged microglia

G, Feature plot of Robo/Slit signaling in all cells of young versus aged hippocampus

Cutoff GO term \log_{10} FDR < 0.5; Cutoff p_{adj} < 0.05 and \log_2 FC > 0.15 for differential gene expression

Single nucleus ATAC sequencing of hippocampi from young and aged mice identifies shifts in oligodendrocyte and microglia subpopulations

Given that deterioration of DNA fidelity is one of the characterized hallmarks of aging, we wished to interrogate the chromatin landscape in the aged hippocampus. Using an independent cohort, we utilized single nucleus ATAC sequencing (snATAC seq), which assays accessible chromatin using a transposase method followed by deep sequencing (Trevino et al., 2021) (Figure 5A). Utilizing known cell type markers as in RNA sequencing above, we were able to use accessible chromatin to identify cell types in young and aged hippocampi. After k-means clustering and dimensionality reduction, we found the known cell types of the hippocampus (Figure 5B). Interestingly, we found that while most cell types clustered together, both oligodendrocytes and microglia clustered by age and cell type (Figure 5C). While the chromatin landscape looked similar between young and aged neurons, there is an immense shift in chromatin accessibility between young and aged microglia and oligodendrocytes (Figure 5D).

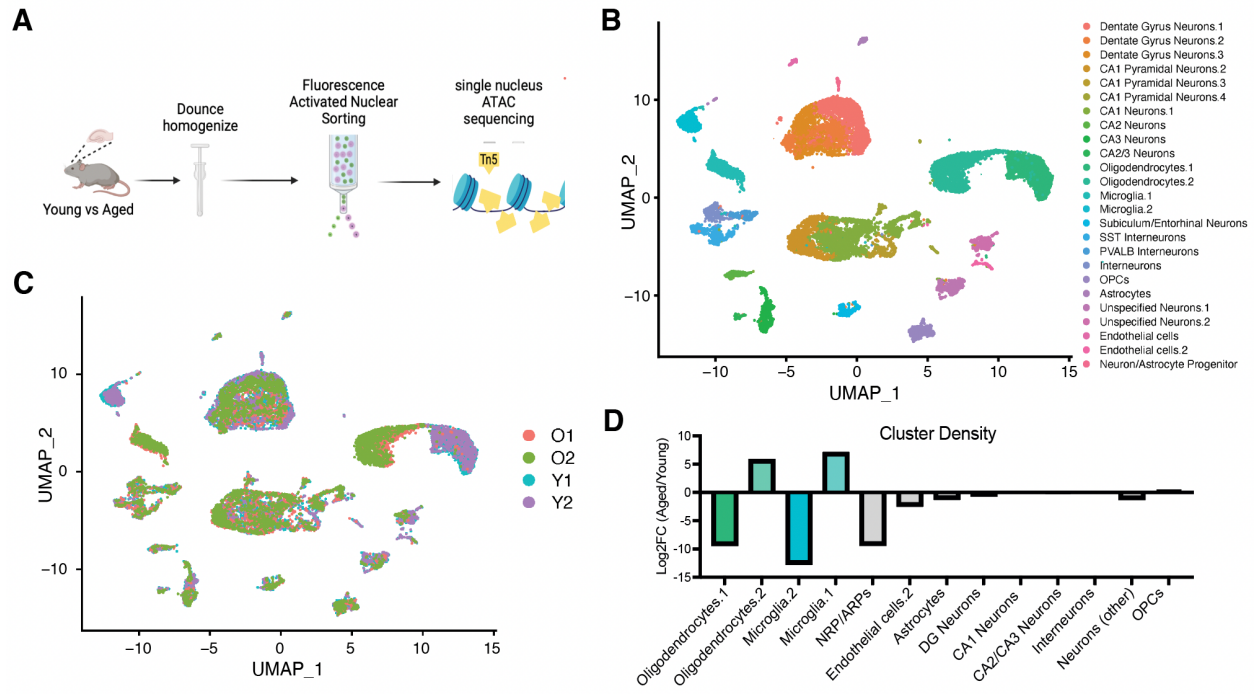


Figure 5. Single nucleus ATAC sequencing from young and aged mice identifies shifts in oligodendrocyte and microglia subpopulations.

A, Schematic illustrating the paradigm for single nucleus ATAC sequencing from hippocampi of young (3mo) and aged (20mo) mice.

B, UMAP projection of 18,686 cells clustered by cell type

C, UMAP projection of 18,686 cells labeled as young (Y1, Y2) or aged (O1, O2)

D, Changes in hippocampal cell subpopulations in aged vs young mice.

Cell type specific changes in chromatin accessibility between young and aged mice.

We observed thousands of differentially accessible peaks (DARs) in both oligodendrocytes and microglia with age (Stuart et al., 2021). We further interrogated the nature of these DARs and found that, in oligodendrocytes, there was an equal number of opening and closing peaks with age (Figure 6A). When we further analyzed peaks opening with age, we found that complement 4B, the gene most highly upregulated in oligodendrocytes with age (Figure 6C), was one of the peaks most significantly opened between aged and young mice (Figure 6B). In contrast, microglia exhibited mostly an opening of chromatin with age. However, of the peaks that did close with age (15% of DARs), most of these genes were histone related (Figure 6D, 6E). The regions that opened were around inflammation-related genes (Figure 6F). We ran a motif enrichment analysis on the DARs of both oligodendrocytes and microglia. The top hits for oligodendrocytes included DNA organization-related transcription factors such as YY1, which regulates enhancer promoter looping (Weintraub et al., 2017). There were significantly less accessible motifs for these transcription factors in aged oligodendrocytes (Figure 6G). In microglia, there were increased accessible consensus motifs for inflammation-related transcription factors such as PU.1 and Izkf1 (Figure 6H). Interestingly, an analysis of Alzheimer's Disease postmortem brain tissue also found PU.1 as a top differentially accessible motif, indicating this may be a shared pathway between age-related cognitive decline and neurodegenerative disease (Morabito et al., 2021).

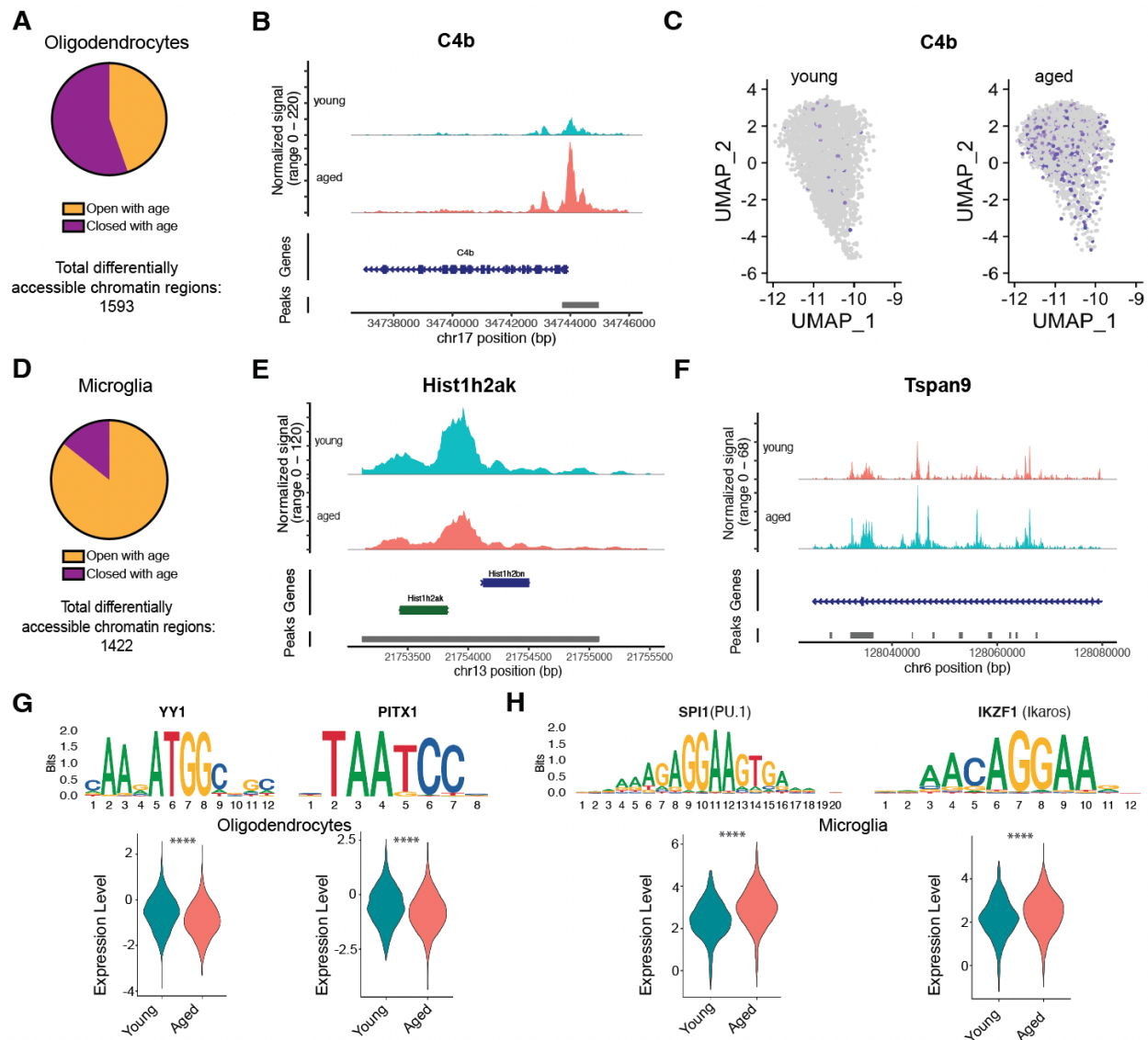


Figure 6. Analysis of differentially accessible regions in aging oligodendrocytes and microglia

A, Pie chart depicting changes in chromatin accessibility in oligodendrocytes
B, Genome track around differentially accessible peak region in oligodendrocytes
C, Feature plot of snRNA-seq of C4b in oligodendrocytes with age
D, Pie chart depicting changes in chromatin accessibility in microglia
E, Genome track around differentially accessible peak region in oligodendrocytes
F, Genome track around differentially accessible peak region in oligodendrocytes
G, Violin plot of enrichment of top motifs differentially accessible in oligodendrocytes with age
H, Violin plot of enrichment of top motifs differentially accessible in microglia with age
(p adj < 0.0001 for all motifs listed. N = 2, Analysis in Signac)

Transcriptome analysis of hippocampi from aged exercise mice reveal rejuvenation pathways

In order to interrogate the molecular mechanisms of rejuvenation, we performed snRNA seq on hippocampi from aged exercised mice (Figure 7A). This group was in the same experiment as the young and aged dataset, and this could serve as a control. The UMAP projection shows no drastic change in cell count or clustering (Figure 7B). We find that there are much fewer differentially expressed genes with exercise than with aging, similar to other rejuvenation paradigms (Pálovics et al., 2022). However, when we survey top genes that were differentially expressed between aged and exercised mice, we find a number of these genes reverting to more youthful levels (Figure 7C). We find that there is indeed a rejuvenation program in transcriptional output in exercised mice that we hope to leverage for therapeutic benefit.

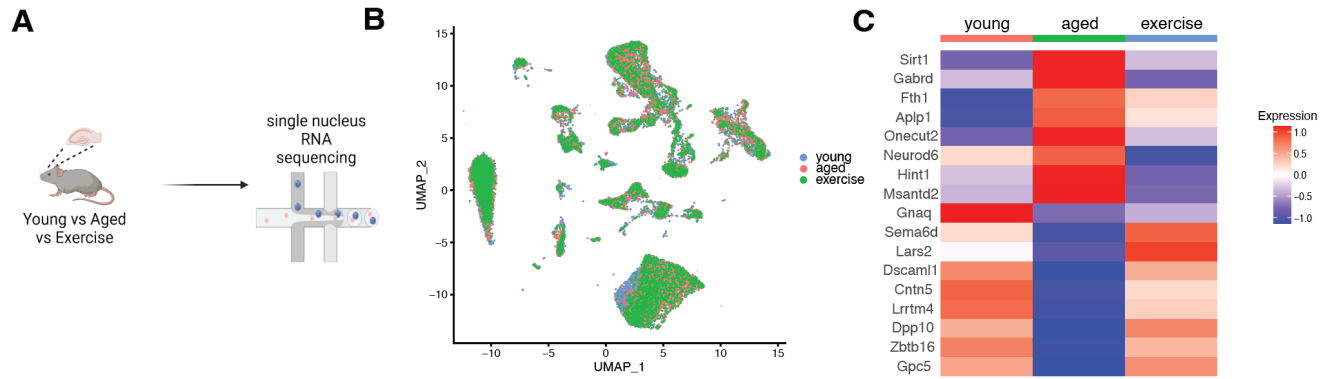


Figure 7. snRNA-seq of exercised mice identifies potential rejuvenation profile in the aging hippocampus.

A, Schematic illustrating the paradigm for snRNA-seq from hippocampi dissected from young (3mo), aged (22mo) mice, and aged exercised (22mo) mice.

B, UMAP projection of 35,037 nuclei labeled by sample type.

C, Heat map of several top differentially expressed genes between all nuclei of young, aged, and aged exercised hippocampi (n=2/group). Differential expression testing by Seurat – Cutoff, p-adjusted < 0.05.

DISCUSSION

Here we report the first cross-sectional study of cognitive function across the mouse lifespan. We found that cognitive decline was temporally heterogeneous across modalities, within subjects, and between subjects. Future work will include analysis of snRNA-seq and snATAC-seq from all hippocampi of the 72 mice that underwent cognitive testing. We hope to find meaningful correlations between cognitive function and transcriptional output by interrogating aged mice that are cognitively resilient, young mice, and aged mice that exhibited severe cognitive decline. We wish to understand the molecular mechanisms underlying cognitive decline across different modalities and different subjects to see if we can make associations between transcription and cognitive performance. With this, we hope to find key gene regulatory networks involved in specific aspects of age-related cognitive decline, and interestingly, key networks in cognitive resilience with age. We wish to then test some of these key genes by manipulating levels in the mouse model. To answer this question, we collaborated with Stanford University to perform bulk RNA sequencing on all different brain regions across all 72 mice from this study.

As bookends, we performed snRNA and snATAC seq as proof-of-concept studies. We were able to identify key known aging signatures in different cell types, while also identifying novel potential regulatory pathways. One limitation in this study is that we don't have adequate representation of astrocytes in our data. Interestingly, oligodendrocytes exhibited the most aberrant transcription with age, as well as a severe difference in the chromatin landscape. Key transcription factors that maintain DNA structure had fewer consensus motifs to bind to with age, indicating a breakdown in DNA integrity and thus aberrant transcriptional output. Dentate gyrus neurons had decreased gene expression in synaptic plasticity pathways, and microglia had increased cell activation, which was mirrored in the chromatin accessibility analysis. Perhaps targeting transcription factors identified in the snATAC-seq data could revert different cell types to more youthful states. Further work will include integrating our exercise-induced rejuvenation

data to find key gene regulatory networks and transcription factors to potentially target for rejuvenation.

In conclusion, we report here an aging timecourse of cognitive function across the mouse lifespan. We then perform hippocampus-specific snRNA seq and snATAC seq and find important transcriptional changes with age, as well as changes in DNA accessibility, particularly in oligodendrocytes. Future work will find key links between molecular mechanisms and age-related cognitive decline.

Materials and Methods

Animal Models. All mouse handling and use was in accordance with institutional and ethical guidelines approved by the University of California San Francisco (UCSF) IACUC. For this study, C57BL/6 male mice (The Jackson Laboratory) were ordered at the following ages: 6 weeks, 18 weeks, 42 weeks, 66 weeks, and 90 weeks old. Mice were housed at UCSF for three weeks and handled for one week before undergoing behavioral testing. The numbers of mice used to result in statistically significant differences were calculated using standard power calculations with $\alpha = 0.05$ and a power of 0.8. We used an online tool (<http://www.stat.uiowa.edu/~rlenth/Power/index.html>) to calculate power and samples size based on experience with the respective tests, variability of the assays and inter- individual differences within groups. Mice were housed under specific pathogen-free conditions under a 12 h light-dark cycle. All experiments were randomized and blinded by an independent researcher. Researchers remained blinded throughout molecular and behavioral assessments. Groups were un-blinded at the end of each experiment upon statistical analysis.

Open Field. Mice were placed in the center of an open 40cm x 40cm square chamber (Kinder Scientific) with no cues or stimuli and allowed to move freely for 10 minutes. Infrared photobeam breaks were recorded and movement metrics analyzed by MotorMonitor software (Kinder Scientific).

Novel Object Recognition. The novel object recognition task was performed according to the protocol previously described (White et al., 2020). During the habituation phase (day 1), mice could freely explore an empty arena for 10 minutes. During the training phase (day 2), two identical objects were placed in the habituated arena, and mice could explore the objects for 5 minutes. For the testing phase (day 3), one object was replaced with a novel object, and mice could explore the objects for 5 minutes. Time spent exploring each object was quantified using

the Smart Video Tracking Software (Panlab; Harvard Apparatus). Two different sets of objects are used. To control for any inherent object preference, half of the mice are exposed to object A as their novel object and half to object B. To control for any potential object-independent location preference, the location of the novel object relative to the trained object is also varied. The objects were chosen based on their ability to capture the animal's interest, independent of genetic background or age. To determine percent time with novel object, we calculate $(\text{Time with novel object}) / (\text{Time with Trained Object} + \text{Time with Novel Object}) * 100$. In this preference index, 100% indicates full preference for the novel object, and 0% indicates full preference for the trained object. A mouse with a value of 50% would have spent equal time exploring both objects. Mice that did not explore both objects during the training phase were excluded from analysis.

Radial arm water maze. Spatial learning and memory was assessed using the radial arm water maze (RAWM) paradigm according to the protocol previously described (Alamed et al., 2006). In this task the goal arm location containing a platform remains constant throughout the training and testing phase, while the start arm is changed during each trial. Spatial cues are posted on all four walls of the RAWM area. Entry into an incorrect arm is scored as an error, and errors are averaged over training blocks (three consecutive trials). On day one, during the training phase, mice are trained for 15 trials, with trials alternating between a visible and hidden platform for blocks 1-4 and then switching to only a hidden platform in block 5. On day 2 during the testing phase, mice are tested for 15 trials with a hidden platform for blocks 6-10. Investigators were blinded to genotype and treatment when scoring.

snRNA sequencing. Droplet-based single nucleus RNA-sequencing (snRNA seq) on isolated nuclei was conducted based on a protocol generated by 10x Genomics with the following modifications. Subdissected hippocampi were dounce homogenized 15x with a loose pestle and 20x with a tight pestle in NP-40 Lysis Buffer (10mM Tris-HCl, 10mM NaCl, 3mM MgCl₂, 0.1% Nonidet P40 Substitute, 1mM DTT, 1U/ul RNase Inhibitor). Samples were incubated for 7 min on

ice and pipette mixed a few times during incubation with a wide-bore pipette tip. Samples were passed through a 35 μm strainer to a 2-ml microcentrifuge tube and centrifuged at 500 RCF for 5 min at 4°C. After removing most of the supernatant, we added 1 ml PBS + 1% BSA + 1U/ μl RNase Inhibitor and incubated undisturbed for 5 min on ice. We pipette mixed to resuspend the pellet, centrifuged at 500 rcf for 5 min at 4°C, and removed the supernatant. Pellets resuspended in 1ml PBS + 1% BSA + 1U/ μl RNase Inhibitor and Hoescht 33342 (1:10,000) for Fluorescence Activated Nuclear Sorting (FANS) on a BD FACSAria II. DAPI+ singlet nuclei were sorted into 1 ml PBS + 1% BSA + 1U/ μl RNase Inhibitor, spun down at 500 RCF for 5 min at 4°C, and resuspended and counted for submission to library preparation. 30,000 nuclei were loaded on to the 10x Chromium Single Cell 3' v3. The Institute for Human Genetics Core at UCSF then prepared libraries and sequenced using S4 lanes of a NovaSeq 6000 Illumina sequencer. Data was analyzed using CellRanger software (v.4.0.0) (10x Genomics) for mm10 genome alignment and Seurat 4.0 for Principal Component Analysis, k-means clustering, and downstream differential gene expression analysis.

Data and statistical analysis. Graphed data are expressed as mean \pm SEM. Statistical analysis was performed with Prism 9.0 software (GraphPad Software). Means between two groups were compared with two-tailed, unpaired Student's t-test. Comparisons of means from multiple groups with each other or against one control group were analyzed with 2-way ANOVA and Bonferroni post hoc tests. All behavior experiments conducted were done in a randomized and blinded fashion. For each experiment, the overall size of the experimental groups corresponded to distinct animals. Unique samples were not measured repeatedly within the same characterization of a given cohort.

REFERENCES

Allen, W. E., Blosser, T. R., Sullivan, Z. A., Dulac, C., & Zhuang, X. (2023). Molecular and spatial signatures of mouse brain aging at single-cell resolution. *Cell*, 186(1), 194-208.e18. <https://doi.org/10.1016/j.cell.2022.12.010>

Bieri, G., Schroer, A. B., & Villeda, S. A. (2023). Blood-to-brain communication in aging and rejuvenation. *Nature Neuroscience*, 26(3), 379–393. <https://doi.org/10.1038/s41593-022-01238-8>

Deczkowska, A., Keren-Shaul, H., Weiner, A., Colonna, M., Schwartz, M., & Amit, I. (2018). Disease-Associated Microglia: A Universal Immune Sensor of Neurodegeneration. *Cell*, 173(5), 1073–1081. <https://doi.org/10.1016/j.cell.2018.05.003>

Fan, X., Wheatley, E. G., & Villeda, S. A. (2017). Mechanisms of hippocampal aging and the potential for rejuvenation. *Annual Review of Neuroscience*, 40, 251–272. <https://doi.org/10.1146/annurev-neuro-072116-031357>

Gonzales, M. M., Garbarino, V. R., Pollet, E., Palavicini, J. P., Kellogg, D. L., Kraig, E., & Orr, M. E. (2022). Biological aging processes underlying cognitive decline and neurodegenerative disease. *The Journal of Clinical Investigation*.

Horowitz, A. M., Fan, X., Bieri, G., Smith, L. K., Sanchez-Diaz, C. I., Schroer, A. B., Gontier, G., Casaletto, K. B., Kramer, J. H., Williams, K. E., & Villeda, S. A. (2020). Blood factors transfer beneficial effects of exercise on neurogenesis and cognition to the aged brain. *Science*, 369(6500), 167–173. <https://doi.org/10.1126/science.aaw2622>

López-Otín, C., Blasco, M. A., Partridge, L., Serrano, M., & Kroemer, G. (2013). The hallmarks of aging. *Cell*, 153(6), 1194–1217. <https://doi.org/10.1016/j.cell.2013.05.039>

Morabito, S., Miyoshi, E., Michael, N., Shahin, S., Martini, A. C., Head, E., Silva, J., Leavy, K., Perez-Rosendahl, M., & Swarup, V. (2021). Single-nucleus chromatin accessibility and transcriptomic characterization of Alzheimer's disease. *Nature Genetics*, 53(8), 1143–1155. <https://doi.org/10.1038/s41588-021-00894-z>

Nyberg, L., Lövdén, M., Riklund, K., Lindenberger, U., & Bäckman, L. (2012). Memory aging and brain maintenance. *Trends in Cognitive Sciences*, 16(5), 292–305. <https://doi.org/10.1016/j.tics.2012.04.005>

Pálovics, R., Keller, A., Schaum, N., Tan, W., Fehlmann, T., Borja, M., Kern, F., Bonanno, L., Calcuttawala, K., Webber, J., McGeever, A., Tabula Muris Consortium, Luo, J., Pisco, A. O., Karkanas, J., Neff, N. F., Darmanis, S., Quake, S. R., & Wyss-Coray, T. (2022). Molecular hallmarks of heterochronic parabiosis at single-cell resolution. *Nature*, 603(7900), 309–314. <https://doi.org/10.1038/s41586-022-04461-2>

Satija, R., Farrell, J. A., Gennert, D., Schier, A. F., & Regev, A. (2015). Spatial reconstruction of single-cell gene expression data. *Nature Biotechnology*, 33(5), 495–502. <https://doi.org/10.1038/nbt.3192>

Stuart, T., Srivastava, A., Madad, S., Lareau, C. A., & Satija, R. (2021). Single-cell chromatin state analysis with Signac. *Nature Methods*, 18(11), 1333–1341. <https://doi.org/10.1038/s41592-021-01282-5>

Trevino, A. E., Müller, F., Andersen, J., Sundaram, L., Kathiria, A., Shcherbina, A., Farh, K., Chang, H. Y., Paşca, A. M., Kundaje, A., Paşca, S. P., & Greenleaf, W. J. (2021). Chromatin and gene-regulatory dynamics of the developing human cerebral cortex at single-cell resolution. *Cell*, 184(19), 5053-5069.e23. <https://doi.org/10.1016/j.cell.2021.07.039>

Weintraub, A. S., Li, C. H., Zamudio, A. V., Sigova, A. A., Hannett, N. M., Day, D. S., Abraham, B. J., Cohen, M. A., Nabet, B., Buckley, D. L., Guo, Y. E., Hnisz, D., Jaenisch, R., Bradner, J. E., Gray, N. S., & Young, R. A. (2017). YY1 Is a Structural Regulator of Enhancer-Promoter Loops. *Cell*, 171(7), 1573-1588.e28. <https://doi.org/10.1016/j.cell.2017.11.008>

Ximerakis, M., Lipnick, S. L., Innes, B. T., Simmons, S. K., Adiconis, X., Dionne, D., Mayweather, B. A., Nguyen, L., Niziolek, Z., Ozek, C., Butty, V. L., Isserlin, R., Buchanan, S. M., Levine, S. S., Regev, A., Bader, G. D., Levin, J. Z., & Rubin, L. L. (2019). Single-cell transcriptomic profiling of the aging mouse brain. *Nature Neuroscience*, 22(10), 1696–1708. <https://doi.org/10.1038/s41593-019-0491-3>

Zalocusky, K. A., Najm, R., Taubes, A. L., Hao, Y., Yoon, S. Y., Koutsodendris, N., Nelson, M. R., Rao, A., Bennett, D. A., Bant, J., Amornkul, D.-E. J., Xu, Q., An, A., Cisne-Thomson, O., & Huang, Y. (2021). Neuronal ApoE upregulates MHC-I expression to drive selective neurodegeneration in Alzheimer's disease. *Nature Neuroscience*, 24(6), 786–798. <https://doi.org/10.1038/s41593-021-00851-3>

Chapter 2

Loss of neuronal Tet2 enhances hippocampal-dependent cognitive function

Karishma J. B. Pratt^{1,2} Jeremy M. Shea¹, Laura Remesal-Gomez¹, Gregor Bieri¹, Lucas K. Smith^{1,3}, Julien Couthouis⁴, Christopher P. Chen², Irena J. Roy², Geraldine Gontier^{1#} and Saul A. Villeda^{1-3,5-7}

1. Department of Anatomy, University of California San Francisco, San Francisco, California 94143, USA
2. Developmental and Stem Cell Biology Graduate Program, University of California San Francisco, San Francisco, California 94143, USA
3. Biomedical Sciences Graduate Program, University of California San Francisco, San Francisco, California 94143, USA
4. Department of Genetics, Stanford University School of Medicine, Stanford California, 94305, California, USA
5. Department of Physical Therapy and Rehabilitation Science, San Francisco, California 94143, USA
6. Bakar Aging Research Institute, San Francisco, California, 94143, USA
7. Lead Contact

Author Contributions:

K.J.B.P, J.M.S, G.G. and S.A.V. developed concept and designed experiments. K.J.B.P. performed *in vitro*, *in vivo*, and molecular studies. J.M.S. performed molecular studies. G.G. performed *in vivo* studies. L.R-G., G.B, L.K.S, J.C, C.C and I.J.R. assisted with *in vitro*, *in vivo* and molecular studies. K.J.B.P., J.M.S, and S.A.V. wrote the manuscript. G.G. and S.A.V. supervised all aspects of the project. All authors had the opportunity to discuss results and comment on the manuscript.

Abstract

DNA methylation has emerged as a critical modulator of neuronal plasticity and cognitive function. Notwithstanding, the role of enzymes that demethylate DNA remain to be fully explored. Here, we report that loss of ten-eleven translocation methylcytosine dioxygenase 2 (Tet2), which catalyzes oxidation of 5-methylcytosine (5mC) to 5-hydroxymethylcytosine (5hmC), in adult neurons enhances cognitive function. In the adult mouse hippocampus, we detected an enrichment of Tet2 in neurons. Viral-mediated neuronal overexpression and RNA interference of Tet2 altered dendritic complexity and synaptic-plasticity-related gene expression in vitro. Overexpression of neuronal Tet2 in adult hippocampus, and loss of Tet2 in adult glutamatergic neurons, resulted in differential hydroxymethylation associated with genes involved in synaptic transmission. Functionally, overexpression of neuronal Tet2 impaired hippocampal-dependent memory, while loss of neuronal Tet2 enhanced memory. Ultimately, these data identify neuronal Tet2 as a molecular target to boost cognitive function.

Introduction

5-methyl-cytosine (5mC) has been considered the fifth base due to its distinct ability to regulate transcription (Jaenisch and Bird, 2003). Specifically, methylated cytosine can disrupt transcription and is responsible for proper inhibition of many genomic regions including imprinted genes, X chromosome inactivation, and transposable elements. Methylated cytosine has also been shown to play a role in gene activation depending on the regulatory element where cytosine is, indicating that methylation plays a nuanced but critical role in transcription.

Although the critical role for epigenetic mechanisms in development and cell differentiation has long been appreciated, recent evidence reveals that these mechanisms are also employed in postmitotic neurons during learning and memory. Modification of DNA by methylation is dynamically regulated in mature neurons to enable processes necessary for cognition (Moore et al., 2013). DNA methylation changes occur in mature neurons at activity-dependent genes following learning paradigms, after synchronous activation by electroconvulsive stimulation, and in response to cognitive enhancement interventions such as exercise (Miller and Sweatt, 2007) (Guo et al., 2011). Thus, in contrast to the previous belief that DNA methylation is a highly stable modification in terminally differentiated cells, dynamic methylation plays an important role in the neuronal function.

Cytosine is methylated by DNA methyltransferases (DNMTs), which can either work *de novo* (DNMT3s) to add methylation to unmethylated DNA or maintain methylation (DNMT1) through a replication process by adding to hemi-methylated DNA. Mice lacking the DNA methyltransferases DNMT1 and DNMT3a in mature forebrain excitatory neurons exhibit deficits in hippocampal-dependent learning and memory (Feng et al., 2010). Conversely, induction of DNMT3a in mature neurons improves memory in aged mice, indicating that increased methylation enhances engram stability (Gulmez Karaca et al., 2020). Much less is known about the functional consequences of demethylation in mature neurons.

TET1-3 iteratively oxidize 5-methyl-Cytosine (5mC) to produce three stepwise intermediates, 5-hydroxymethyl-Cytosine (5hmC), 5-formyl-Cytosine (5fC) and 5-carboxyl-Cytosine (5caC) that can be converted back to cytosine (Tahiliani et al., 2009, Ito et al., 2011) (Figure 1). 5hmC is enriched in the brain, predominantly in neurons and on exon boundaries of active synaptic genes in humans and mice (Kriaucionis and Heintz, 2009, Khare et al., 2012). Correlative studies have indicated that 5hmC may be involved in neuronal function, with health interventions such as caloric restriction resulting in decreased 5hmC in the brain (Chouliaras et al., 2012), while patients with the neuropsychiatric disorder schizophrenia have increased 5hmC (Dong et al., 2012).

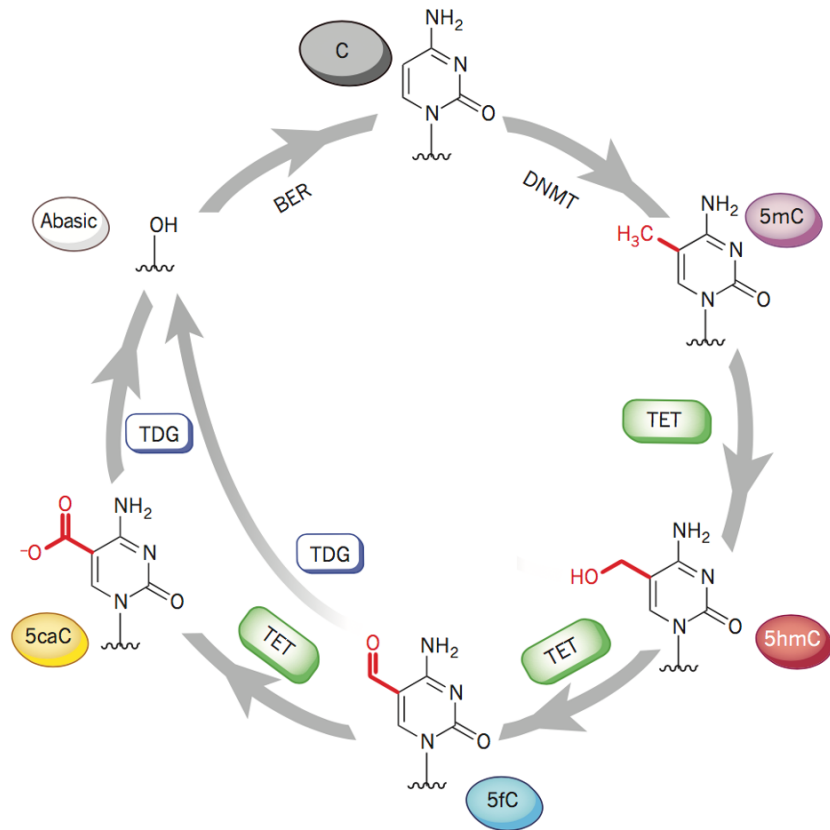


Figure 1. Methylation and demethylation of cytosine. Schematic representing the enzymes required and chemical modifications made to the base pair cytosine (C). Adapted from Kohli and Zhang, 2013.

In the hippocampus, TET enzymes have emerged as critical regulators of cognitive function. Constitutive loss of Tet1 impairs memory extinction in young mice (Rudenko et al., 2013, Kaas et al., 2013), and knockdown of Tet3 in primary hippocampal neurons reduces glutamatergic synaptic scaling and plasticity (Yu et al., 2015). We and others have shown that age-related loss of Tet2 in adult neural stem cells promotes impairments in adult hippocampal neurogenesis and associated cognitive processes (Gontier et al., 2018, Li et al., 2017). However, the functional role of Tet2 in mature neurons remains unexplored.

While decreased TET expression has been implicated in cognitive impairments, here we report that loss of Tet2 in adult mature excitatory forebrain neurons enhances hippocampal-dependent memory. Using *in vitro* and *in vivo* viral-mediated neuronal overexpression and RNA interference approaches, neuron-specific conditional genetic knockout mouse models, RNA sequencing (RNA-Seq) and antibody-based 5hmC immunoprecipitation combined with deep sequencing (hMeDIP-Seq) approaches, we identified differentially expressed genes and hydroxymethylated regions in genes relating to synaptic processes. Increased neuronal Tet2 impaired hippocampal-dependent memory while loss of neuronal Tet2 enhanced memory. These findings indicate that Tet2-mediated neuronal hydroxymethylation and transcriptional changes negatively regulate adult hippocampal synaptic and cognitive processes.

RESULTS

Tet2 mRNA expression is enriched in hippocampal neurons.

Given neuronal enrichment of 5hmC in the brain (Szulwach et al., 2011) (Globisch et al., 2010), we first characterized *Tet2* mRNA expression in NeuN-positive neurons, GFAP-positive astrocytes and IBA1-positive microglia by RNAScope in combination with immunohistochemical analysis of cell markers. We detected a significant enrichment of *Tet2* in adult neurons compared to other cell types (Figure 2).

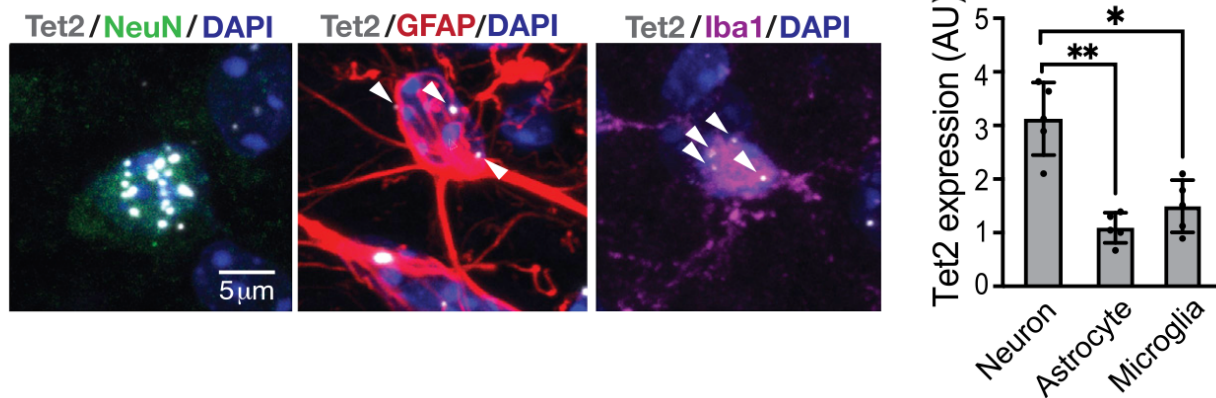


Figure 2. Tet2 is enriched in neurons and regulates neuronal complexity.

Representative image and quantification of *Tet2* RNA scope expression in hippocampal neurons, astrocytes and microglia of young (3 months) adult mice. (n=5 mice with 20-40 cells per animal; one-way ANOVA; *p<0.05, **p<0.01)

Tet2 alters neuronal morphology *in vitro*.

We next investigated the role of neuronal *Tet2* using an *in vitro* model. We used a cell-type specific viral-mediated overexpression approach in which mature primary mouse neurons were infected with lentiviral constructs encoding either *Tet2* (Tet2 OE) or *GFP* control under the control of the neuron-specific Synapsin1 promoter (Figure 3A). *Tet2* overexpression was confirmed by qPCR (Figure 4A). We assessed cellular changes by immunocytochemical analysis and detected a decrease in dendritic complexity of MAP2-positive neurons overexpressing *Tet2* (Figure 3B). To complement these studies, mature neurons were infected with lentivirus encoding shRNA sequences targeting *Tet2* (shTet2) or luciferase control (shLuc) (Figure 3A). Knockdown of *Tet2* was confirmed by qPCR (Figure 4D). Decreased neuronal *Tet2* expression resulted in an increase in dendritic complexity of MAP2-positive neurons (Figure 3C, Figure 4F). No differences in neuronal cell density or toxicity were observed under overexpression or RNA interference conditions (Figure 4B,C,E,F). These data indicate that *Tet2* promotes morphological changes in mature neurons *in vitro*.

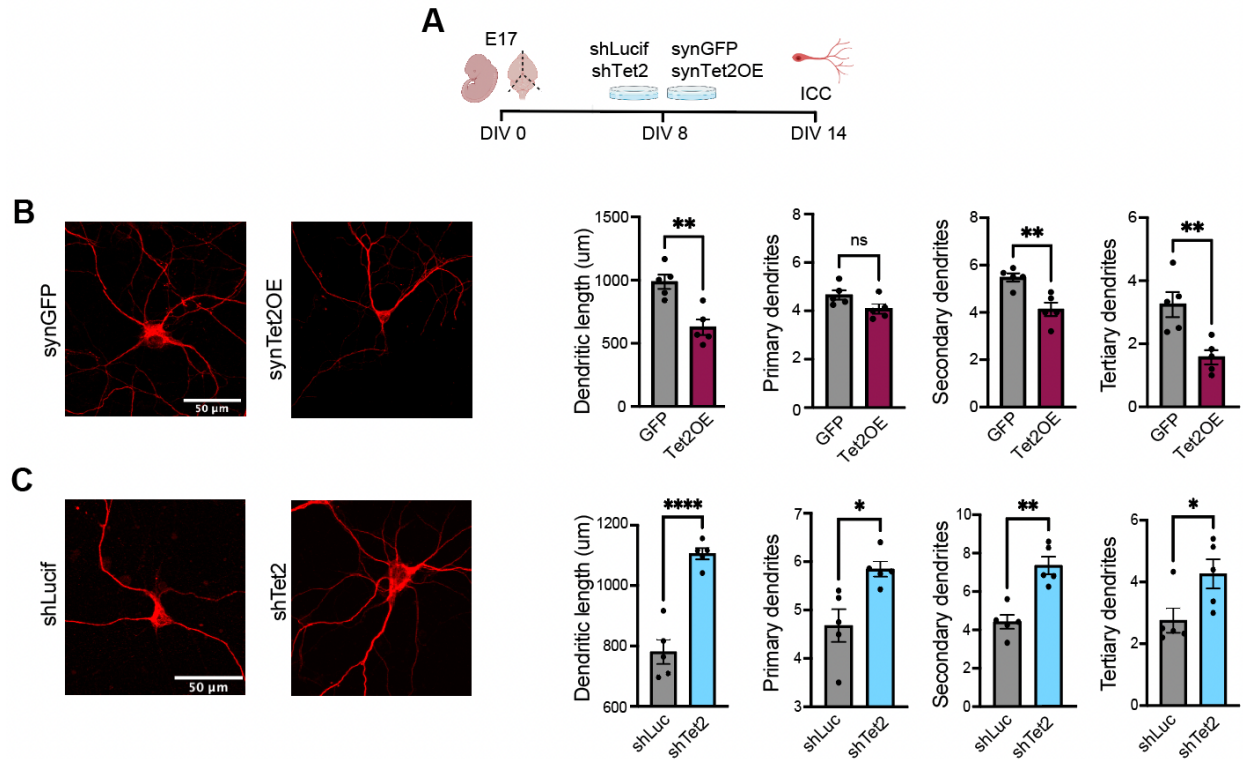


Figure 3. Tet2 regulates neuronal complexity.

A, Schematic of experimental design. Primary mouse neurons were cultured for eight days and subsequently infected with lentivirus encoding *Tet2* (*Tet2* OE) or GFP control sequences under the neuron-specific *Synapsin1* promoter or encoding shRNA sequences targeting *Tet2* (sh*Tet2*) or luciferase control (shCtrl). Cells were analyzed six days after infection.

B, Representative images and quantification of dendritic length and number of primary, secondary and tertiary dendrites for MAP2-positive neurons following viral-mediated *Tet2* overexpression. (n=5 per group; t-test; *p<0.05, **p<0.01)

C, Representative images and quantification of dendritic length and number of primary, secondary and tertiary dendrites for MAP2-positive neurons following viral-mediated *Tet2* knockdown. (n=5 per group; t-test; *p<0.05, **p<0.01, ****p<0.0001)

Data represented as mean +/- SEM.

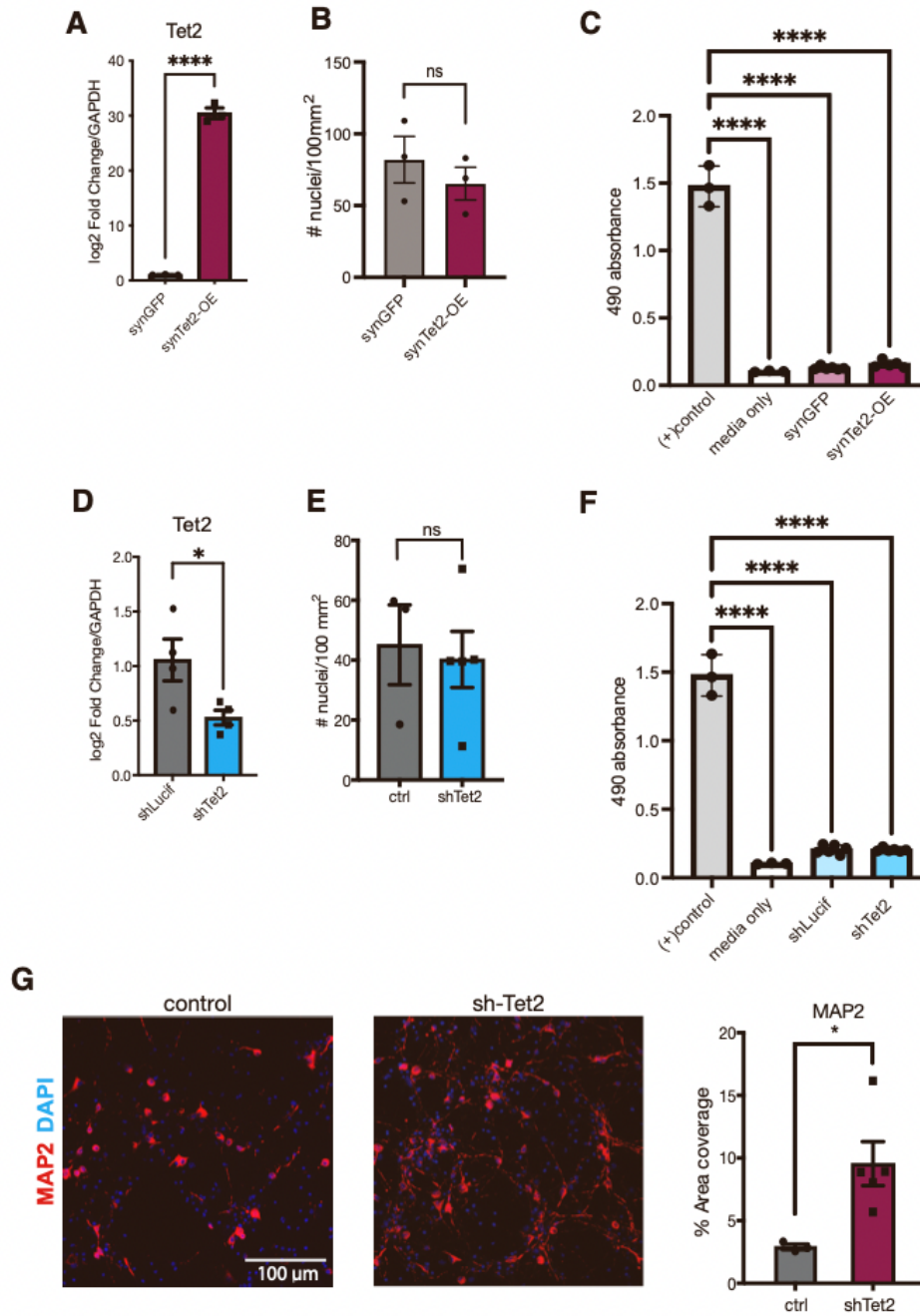


Figure 4. Tet expression and cell viability in primary neurons following neuronal Tet2 overexpression and abrogation.

A, Quantitative reverse-transcription PCR of Tet2 mRNA from primary neurons infected with lentivirus encoding Tet2 (synTet OE) or GFP control (synGFP) under the control of the neuron-specific Synapsin1 promoter. Log2 fold change normalized to GAPDH. (n=3 per group; t-test; *p<0.05).

B, Quantification of number of Hoescht-positive nuclei following Tet2 overexpression (n=3 per group, t-test).

C, Cytotoxicity was measured by lactate dehydrogenase (LDH) activity as relative absorbance following Tet2 overexpression (n=3 per group, t-test).

D, Quantitative reverse-transcription PCR of Tet2 mRNA from primary neurons infected with lentivirus encoding shRNA targeting Tet2 (shTet2) or luciferase control (shCtrl). Log2 fold change normalized to GAPDH. (n=3-4 per group; t-test; *p<0.05)

E, Quantification of number of Hoescht-positive nuclei following Tet2 abrogation (n=3-5 per group, t-test).

F, Cytotoxicity was measured by lactate dehydrogenase (LDH) activity as relative absorbance following Tet2 abrogation (n=5-6 per group, t-test).

G, Representative images and quantification of Immunocytochemistry (ICC) for Map2 expression normalized to number of DAPI-positive nuclei. (n=5 per group; t-test; *p<0.05). Data are represented as mean +/- SEM.

Tet2 alters gene expression profiles of synaptic plasticity-related genes *in vitro*

To gain insight into molecular changes elicited by viral-mediated overexpression and knockdown of *Tet2*, we characterized the neuronal transcriptome by RNA-Seq (Figure 5A). We detected 4,057 differentially expressed genes following *Tet2* overexpression and 3,115 differentially expressed genes following *Tet2* abrogation compared to control conditions. Gene ontology analysis identified processes involved in synaptic vesicle recycling for *Tet2* overexpression (Figure 5B) and synaptic signaling for *Tet2* abrogation (Figure 5D). We surveyed expression of synaptic plasticity genes (Koopmans et al., 2019), and observed bidirectional changes in activity-dependent immediate early genes that included activity regulated cytoskeleton associated protein (*Arc*), early growth response 1 (*Egr1*), neuronal pas domain protein 4 (*Npas4*), and junb proto-oncogene (*JunB*) following *Tet2* overexpression (Figure 5C) and *Tet2* abrogation (Figure 5E). In sum, we detected 552 genes that were bidirectionally changed by *Tet2* overexpression and *Tet2* abrogation (Figure 5F). Gene ontology analysis of the bidirectionally changed gene set identified processes involved in neuronal projection development and regulation of synaptic vesicle recycling (Figure 5G,H). These data raise the possibility that neuronal *Tet2* modulates synaptic signaling and plasticity.

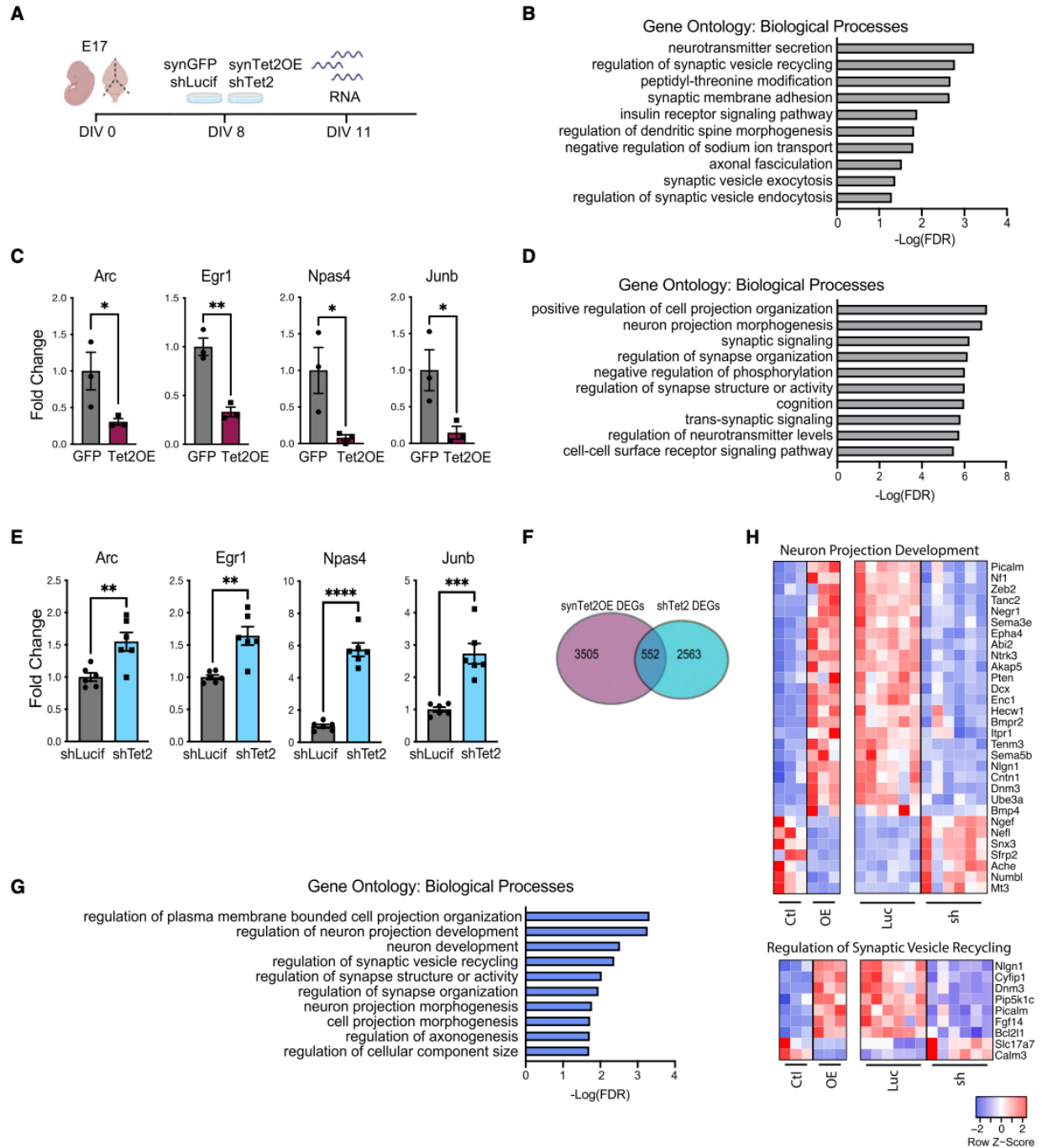


Figure 5. Tet2 regulates synaptic-related gene expression *in vitro*.

A, Schematic of experimental design. Primary mouse neurons were cultured for eight days and infected with lentivirus encoding *Tet2* (Tet2 OE) or GFP control sequences under the neuron-specific Synapsin1 promoter or encoding shRNA sequences targeting *Tet2* (shTet2) or luciferase control (shCtrl).

B, Gene ontology analysis of biological processes on differentially expressed genes between *Tet2* OE and control.

C, Fold change of representative genes from *Tet2* OE RNA-Seq dataset (n=3 per group; adjusted p value with Bonferroni's multiple testing hypothesis correction, *p<0.05, **p<0.01)

D, Gene ontology analysis of biological processes on differentially expressed genes between shTet2 and control.

E, Fold change of representative genes from shTet2 RNA-Seq dataset (n=6 per group; adjusted p value with Bonferroni's multiple testing hypothesis correction, **p<0.01, ***p<0.001, ****p<0.0001)

F, Venn diagram of differentially expressed genes from Tet2 OE and shTet2 RNA-Seq datasets and overlap of bidirectional differentially expressed genes between conditions. Significance threshold set at q<0.05 with absolute fold change >0.5. Overlap p<1.579e-148 by hypergeometric test.

G, Gene ontology analysis of biological process on the 552 genes overlapping between the *Tet2* OE and shTet2 RNA-Seq datasets.

H, Heatmaps of differentially expressed genes from the overlapping gene set in the regulation of neuron projection development (top) and regulation of synaptic vesicle recycling (bottom) biological process categories.

Data represented as mean +/- SEM.

Increased Tet2 in adult hippocampal neurons alters hydroxymethylation on genes related to synaptic transmission and synaptic signaling *in vivo*.

To assess the effect of increasing neuronal *Tet2 in vivo*, young adult wild type mice were given bilateral stereotaxic injections of high-titer virus encoding *Tet2* or *GFP* under the control of the neuron-specific Synapsin1 promoter into their hippocampi (Figure 6A). NeuN-positive neuronal nuclei were isolated by fluorescence activated cell sorting (FACS) from the hippocampi (Figure 7A,B). We used hMeDIP-Seq to assess the influence of *Tet2* overexpression on the DNA hydroxymethylation landscape *in vivo*. Overexpression of *Tet2* in hippocampal neurons led to 270 hMeDIP peaks being gained, while 29 were lost (Figure 6B). Gained hMeDIP peaks were distributed across the genome (Figure 6C) and were enriched in CpG islands, exons, neuronal proximal enhancers, and promoters (Figure 6D), suggesting a functional role in neurons. Performing gene ontology analysis of genes associated with the gained hMeDIP peaks (Figure 6E), we find enrichment of terms related to synaptic transmission, regulation of ion channel activity, and synaptic signaling (Figure 6F). Several of these genes have well-established roles in neuronal function and behavior, such as fibroblast growth factor 14 (*Fgf14*), Slit- and Trk-like protein (*Slitrk2*), and DLG associated protein 2 (*Dlgap2*) (Figure 6G).

To determine the effects of hydroxymethylation changes on gene expression in neurons, we compared our *in vivo* *Tet2* overexpression hMeDIP-Seq dataset to our *in vitro* overexpression and knockdown RNA-Seq datasets (Figure 6H,I). We find that 21 genes that were significantly altered following *Tet2* overexpression *in vitro* also gained hMeDIP peaks with *Tet2* overexpression *in vivo* (Figure 6H), while 23 genes significantly changed following *Tet2* knockdown *in vitro* had associated hMeDIP peaks *in vivo* (Figure 6I). Several of these genes are bidirectionally changed by *Tet2* overexpression and abrogation, and regulate neuronal function, such as *Fgf14*, *Gpm6a*, and *Myo5a*. These results suggest that *Tet2*-mediated hydroxymethylation modulates expression of genes important for neuronal function.

Increased *Tet2* in adult neurons impairs hippocampal-dependent memory.

To investigate the effect of increased neuronal *Tet2* on cognitive processes, hippocampal-dependent learning and memory was assessed using novel object recognition (NOR) and radial arm water maze (RAWM) paradigms in young adult mice following viral-mediated neuronal *Tet2* overexpression in the hippocampus (Figure 6A). During NOR testing, control mice were biased toward a novel object relative to a familiar object, while mice overexpressing neuronal *Tet2* did not show a discrimination toward the novel object (Fig. 6J). In RAWM, all mice showed similar learning capacity during the training phase (Figure 6K). Increased neuronal *Tet2* resulted in significantly more errors in locating the target platform during spatial memory testing compared to control mice (Figure 6K). As a control, we profiled general health using an open field paradigm (Figure 7C) and observed no differences in overall activity, total distance traveled, or time spent in the center of the open field, indicative of normal motor and anxiety functions (Figure 7D). These behavioral data indicate that increased neuronal *Tet2* impairs hippocampal-dependent recognition memory and spatial memory.

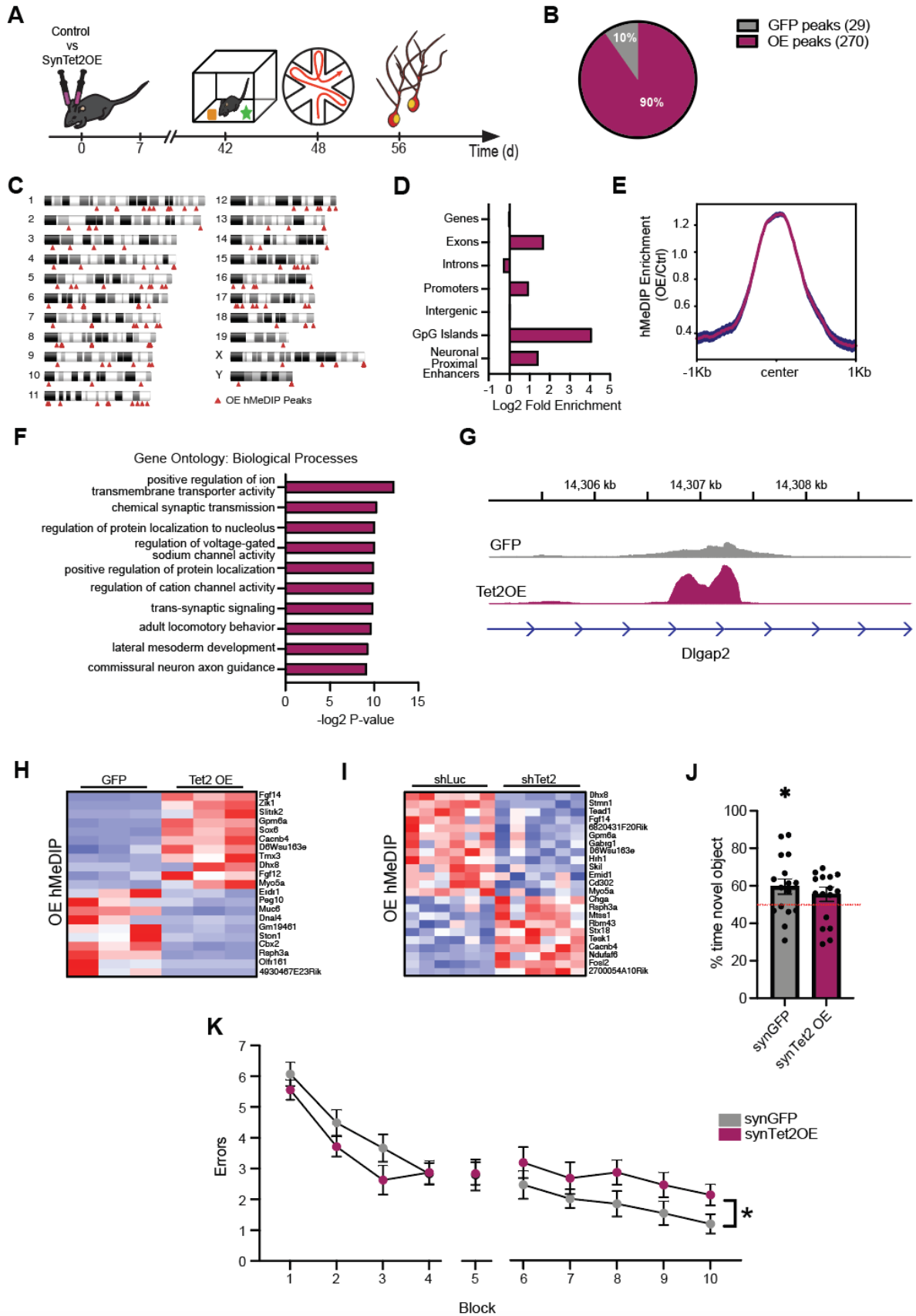


Figure 6. Increased neuronal Tet2 in the adult hippocampus alters hydroxymethylation on genes related to synaptic processes and impairs memory.

A, Schematic of experimental paradigm. Adult (3-4 months) wild type mice were given bilateral stereotaxic injections of lentivirus (LV) encoding either *Tet2* (Tet2 OE) or GFP control sequences driven by the neuron-specific Synapsin1 promoter into the hippocampus and subject to behavioral and molecular analysis 5 weeks later.

B, Pie chart of 5hmC peaks gained (270 peaks) and lost (29 peaks) in Tet2 OE neurons compared to GFP control. ($q=0.05$).

C, Ideogram of genomic location of hMeDIP peaks gained following neuronal Tet2 overexpression.

D, Enrichment of gained hMeDIP peaks over genomic elements in Tet2 OE neurons.

E, Metagene profile of gained hMeDIP peaks following neuronal Tet2 overexpression. Mean +/- SEM.

F, Gene ontology analysis of biological processes on the 131 genes associated with the 270 gained hMeDIP peaks following neuronal Tet2 overexpression.

G, Example gene track of the gained hMeDIP peak associated with *Dlgap2* in Tet2 OE neurons.

H, Heatmap of differentially expressed genes in the *in vitro* Tet2 OE RNA-Seq dataset that have associated gained hMeDIP peaks in the *in vivo* Tet2 OE hMeDIP-Seq dataset.

I, Heatmap of differentially expressed genes in the *in vitro* shTet2 RNA-Seq dataset that have associated gained hMeDIP peaks in the *in vivo* Tet2 OE hMeDIP-Seq dataset.

J, Quantification of percent interaction time during novel object recognition testing (n = 15-16 mice per group; t test, $*p<0.05$).

K, Quantification of the number of entry errors during radial arm water maze training and testing (n=15-16 mice per group; repeated-measures ANOVA with Bonferroni post hoc correction, $*p<0.05$).

Data represented as mean +/- SEM.

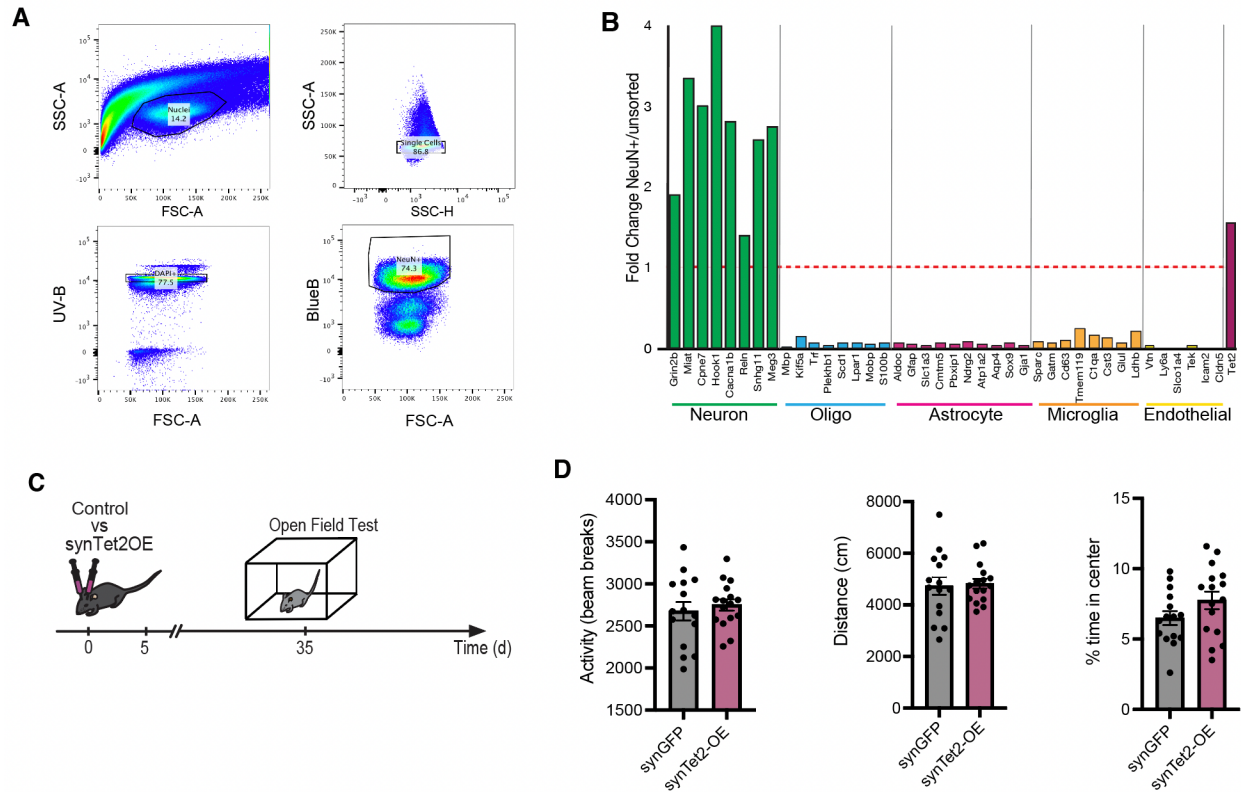


Figure 7. Validation of neuronal nuclei isolation for cell-type specific sequencing analysis and overall health analysis following in vivo viral-mediated neuronal Tet2 overexpression. **A**, Representative fluorescence-activated cell sorting (FACS) gating paradigm for isolation of NeuN-positive neuronal nuclei.

B, Fold change of differentially expressed cell-type specific genes between NeuN-positive nuclei and unsorted lysate from RNA sequencing data (all genes adjusted p value with Bonferroni's multiple testing hypothesis correction, $*p < 0.05$)

C, Schematic of experimental paradigm. Adult (3-4 months) wild type mice were given bilateral stereotaxic injections of lentivirus (LV) encoding either Tet2 (Tet2 OE) or GFP control sequences driven by the neuron-specific Synapsin1 promoter into the hippocampus and subject to behavioral analysis 5 weeks later

D, Overall activity was assessed by open field testing and quantified as distance traveled over 10 minutes. (n=15-16 mice per group; t-test)

Data are represented as mean \pm SEM.

Loss of Tet2 in adult excitatory neurons alters hydroxymethylation on genes related to synaptic transmission and synapse structure *in vivo*.

To investigate the effect of abrogating neuronal *Tet2 in vivo*, we generated *Tet2^{flox/flox}* mice carrying an inducible *CamK2a-Cre-ER^{T2}* gene, in which *Tet2* is excised specifically in adult glutamatergic forebrain neurons upon tamoxifen administration (Tet2 cKO) (Figure 8A). Young adult Tet2 cKO and littermate control (*Tet2^{flox/flox}*) mice were administered tamoxifen and molecular changes were assessed at eight months of age. Decreased *Tet2* expression was confirmed in neuronal nuclei isolated from Tet2 cKO by qPCR (Figure 9A). No differences in *Tet1* and *Tet3* expression were observed between genotypes (Figure 9B). We used hMeDIP-Seq to assess how loss of neuronal *Tet2* affects the DNA hydroxymethylation landscape *in vivo*. We discovered 241 hMeDIP peaks with reduced signal when comparing knockout to wildtype neurons, while there were 103 hMeDIP peaks with augmented signal (Figure 8B). The 241 hMeDIP peaks were distributed across the genome with the most enrichment on chromosomes 9 and X (Figure 8C, Table 3), and overrepresentation at neuronal proximal enhancers (Figure 8D). These 241 hMeDIP peaks are associated with 204 unique genes (Figure 8E). Gene ontology analysis determined an overrepresentation of processes relating to synaptic structure and synaptic transmission for the associated genes (Figure 8F), including neuregulin 3 (*Nrg3*), *Fgf14*, gamma-aminobutyric acid type a receptor of subunit gamma1 (*Gabrg1*), and glutamate ionotropic receptor kainite type subunit 2 (*Grik2*) (Figure 8G). Several genes involved in the identified neuronal processes (Figure 8F) also had hMeDIP peaks that were gained with Tet2 overexpression, such as Smoothed (*Smo*), *Fgf14*, *Gabrg1*, and *Slitrk2*.

To link changes in hydroxymethylation after loss of neuronal *Tet2* to changes in gene expression, we integrated our *in vivo* Tet2 cKO hMeDIP-Seq dataset with our *in vitro* overexpression and knockdown RNA-Seq datasets (Figure 8H,I). hMeDIP peaks lost after deletion of neuronal *Tet2 in vivo* were associated with altered expression of 34 genes following

Tet2 overexpression *in vitro* (Figure 8H) and 29 genes following Tet2 abrogation *in vitro* (Figure 8I). Several of these genes were bidirectionally regulated by opposite Tet2 manipulations, such as *Fgf14*, neuron navigator 3 (*Nav3*), and teneurin transmembrane protein 3 (*Tenm3*). These results indicate that loss of Tet2 reduces DNA hydroxymethylation at neuronally relevant genomic elements with concordant changes in gene expression. Our combined sequencing analysis suggests that Tet2 modulates functionally relevant gene expression programs in neurons through directed hydroxymethylation changes.

Loss of Tet2 in adult excitatory neurons enhances hippocampal-dependent memory.

Behavioral data indicate that increasing neuronal Tet2 in the adult hippocampus impairs memory; however, it remains an open question whether decreasing neuronal Tet2 can enhance cognitive function. Hippocampal-dependent learning and memory was assessed using fear-conditioning and RAWM paradigms in eight-months-old adult Tet2 cKO and littermate control mice (Figure 8A). During fear conditioning training, mice exhibited no differences in baseline freezing time between genotypes (Figure 9B). Loss of neuronal Tet2 resulted in increased freezing time during contextual (Figure 8J), but not cued (Figure 9B), memory testing. In RAWM, all mice showed similar learning capacity during the training phase (Figure 8K). Loss of Tet2 in adult glutamatergic forebrain neurons resulted in significantly less errors in locating the target platform during spatial memory testing compared to control mice (Figure 8K). We observed no differences in general health using an open field paradigm (Figure 9C-F). These data demonstrate that loss of Tet2 in adult excitatory neurons enhances hippocampal-dependent associative fear memory acquisition and spatial memory.

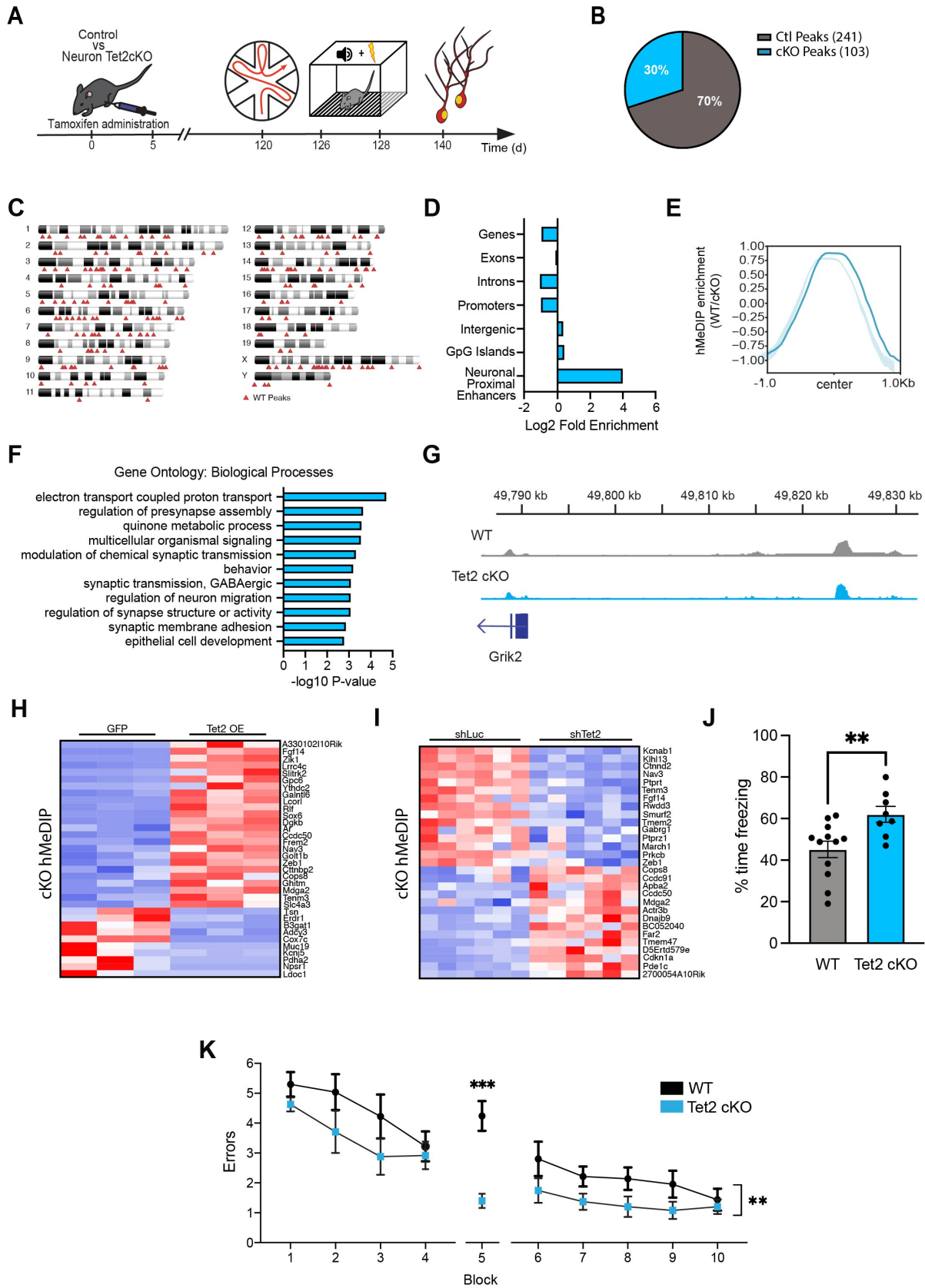


Figure 8. Loss of Tet2 in adult excitatory neurons alters hydroxymethylation on genes related to synaptic processes and enhances hippocampal-dependent memory.

A, Schematic of experimental paradigm. Adult (4 months) CamK2aCre-ER^{T2};Tet2^{flox/flox} excitatory neuron-specific knockout (Tet2 cKO) and littermate Tet2^{flox/flox} control (WT) mice were administered tamoxifen and subject to behavioral and molecular assays after four months.

B, Pie chart of hMeDIP peaks gained (103 peaks) and lost (241 peaks) in Tet2 cKO neurons compared to control. ($q=0.05$).

C, Ideogram of genomic location of hMeDIP peaks lost following loss of neuronal Tet2.

D, Enrichment of lost hMeDIP peaks over genomic elements in Tet2 cKO neurons.

E, Metagene profile of lost hMeDIP peaks following loss of neuronal *Tet2*. Mean +/- SEM.

F, Gene ontology analysis of biological processes on the 202 genes associated with the 241 lost hMeDIP peaks following loss of neuronal *Tet2*.

G, Example gene track of the lost hMeDIP peak associated with *Grik2* in Tet2 cKO neurons.

H, Heatmap of differentially expressed genes in the *in vitro* Tet2 OE RNA-Seq dataset that have associated lost hMeDIP peaks in the *in vivo* Tet2 cKO hMeDIP-Seq dataset.

I, Heatmap of differentially expressed genes in the *in vitro* shTet2 RNA-Seq dataset that have associated lost hMeDIP peaks in the *in vivo* Tet2 cKO hMeDIP-Seq dataset.

J, Quantification of the percentage of freezing 24h after contextual fear conditioning training is shown ($n = 8-12$ mice per group; t test, $**p<0.01$).

K, Quantification of the number of entry errors during radial arm water maze training and testing ($n=8-12$ mice per group; repeated-measures ANOVA with Bonferroni post hoc correction, $**p<0.01$, $***p<0.001$).

Data represented as mean +/- SEM.

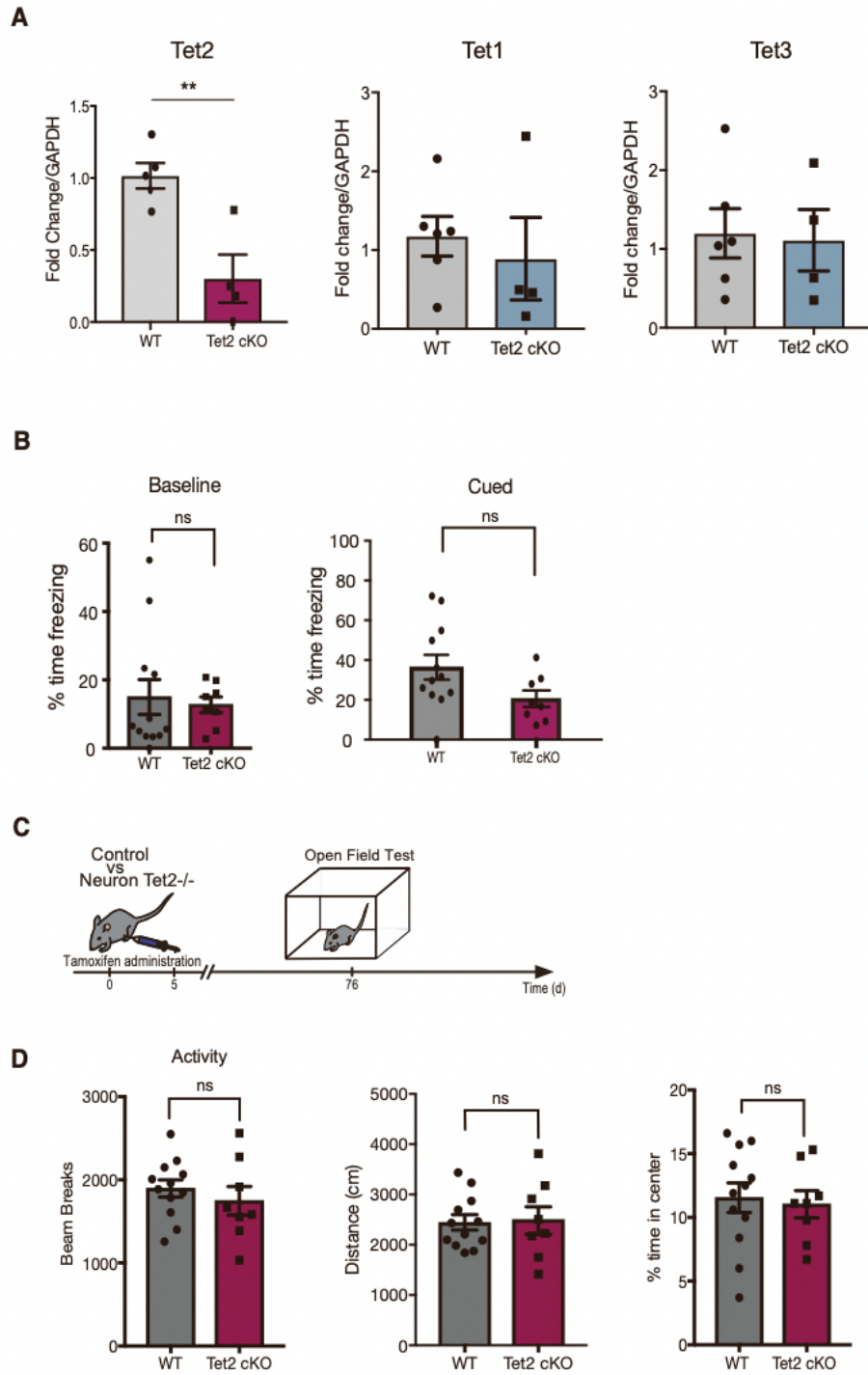


Figure 9. Tet expression and overall health analysis following temporally controlled in vivo loss of neuronal Tet2.

A, Quantitative reverse-transcription PCR of Tet1, Tet2, and Tet3 mRNA from the hippocampus of adult CamK2aCre-ERT2;Tet2 flox/flox (Tet2 cKO) and littermate Tet2 flox/flox control (WT) mice following tamoxifen administration. Log2 fold change normalized to GAPDH. (n=4-5 mice per group; t-test; **p<0.01)

B, Associative fear memory was assessed in Tet2 cKO and WT mice using fear conditioning paradigms. Baseline freezing was quantified as percent freezing in the first two minutes of training. (n=8-12 mice per group; t-test)

C, Tet2 cKO and littermate WT control mice were administered tamoxifen and subject to behavioral assays after four months.

D, Overall activity was assessed by open field testing and quantified as distance traveled over 10 minutes. (n=8-12 mice per group; t-test)

Data are represented as mean +/- SEM.

DISCUSSION

Cumulatively, our data indicate that neuronal Tet2 negatively regulates hippocampal-dependent memory (Figure 10). Our *in vitro* neuronal RNA-Seq data in combination with our *in vivo* neuronal hMeDIP-Seq data dissect the involvement of Tet2 in regulating synaptic processes at the DNA modification and transcriptional level and implicate downstream synaptic plasticity gene targets as cell autonomous regulators of neuronal function. We demonstrate that overexpression of neuronal Tet2 in the hippocampus impairs memory, while loss of neuronal Tet2 in excitatory forebrain neurons enhances hippocampal-dependent memory. Our data identify neuronal Tet2 as a molecular target to boost cognitive function in the adult brain.

Despite similar enzymatic activity, TET enzymes exhibit unique regulatory functions (Rasmussen and Helin, 2016). In the brain, Tet1 regulates neuronal activity and memory formation, with abrogation of Tet1 leading to aberrant long-term depression and impairments in memory extinction (Kaas et al., 2013)(Rudenko et al., 2013). Tet3 regulates glutamatergic synaptic scaling *in vitro*, and knockdown of Tet3 impairs cocaine-induced memory consolidation (Yu et al., 2015)(Liu et al., 2018). In contrast, we show that loss of neuronal Tet2 modulates synaptic gene expression and enhances hippocampal-dependent memory. These differences likely arise from unique genomic targeting of TET family members, particularly as Tet2 lacks a DNA binding domain and is guided by binding partners.

We and others identified a role for adult neural stem cell Tet2 in promoting neurogenesis and enhancing cognition in older mice ([Gontier et al., 2018](#)) (Li et al., 2017). Demethylation processes and Tet2 specifically are required for efficient cell fate decisions and differentiation (Li et al., 2017), with age-related loss of Tet2 in adult neural stem cells inhibiting neurogenesis and impairing associated cognitive processes (Gontier et al., 2018). Our present work investigating the role of neuronal Tet2 in regulating hippocampal-dependent memory complements our

previous findings in adult neural stem cells, highlighting the cell-type specific and context-dependent roles of Tet2 in the adult and aging hippocampus.

Dysregulation of the neuroepigenome, particularly DNA methylation, is a hallmark of brain aging and age-related neurodegenerative disorders (Hwang et al., 2017). Our data supports recent research delineating the role of Tet2 in promoting Alzheimer's disease (Carrillo-Jimenez et al., 2019), and the neuroprotective role of Tet2 loss in Parkinson's disease (Marshall et al., 2020). Cumulatively, this work posits neuronal Tet2 inhibition as an exciting therapeutic approach for age-related cognitive decline.

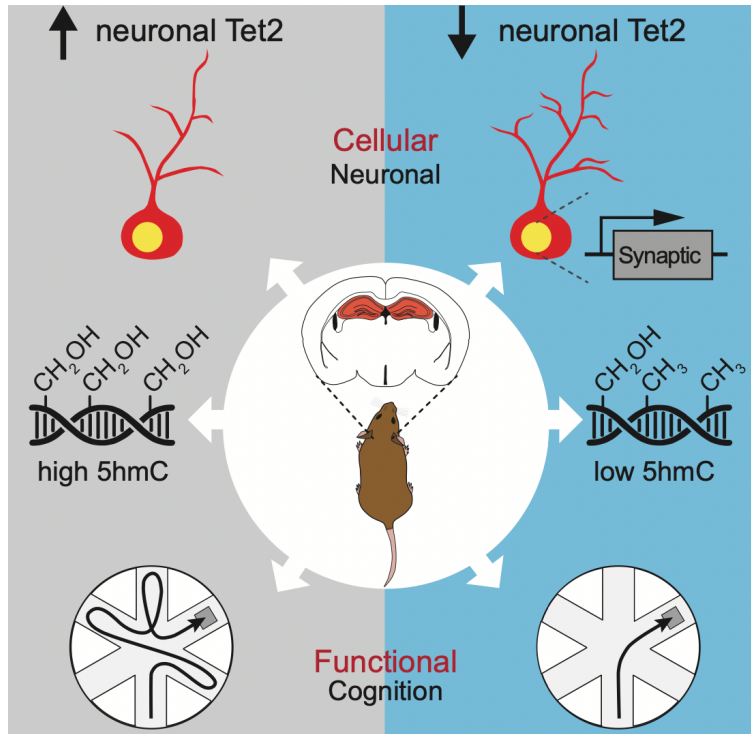


Figure 10. Graphical Abstract of Chapter 2. Graphical Abstract demonstrating findings from Chapter 2. Increased neuronal Tet2 leads to increased hydroxymethylation and impaired memory, while decreased neuronal Tet2 leads to increased expression of immediate early genes, decreased 5hmC, and enhanced memory.

Limitations of the study

While confirmed at the mRNA level, overexpression or knockdown of Tet2 protein was difficult to ascertain using commercially available antibodies. Neuronal *in vivo* hMeDIP-Seq data in combination with *in vitro* RNA-Seq data begin to dissect the involvement of Tet2 in regulating synaptic processes at the transcriptional level. We note that this analysis postulated that 5hmC could be altered similarly *in vitro* and *in vivo* following neuronal Tet2 manipulation. Further hMeDIP-seq analysis of primary neurons is warranted to gain a full understanding of the convergent changes in neuronal 5hmC following Tet2 manipulation *in vitro* versus *in vivo*. Additionally, *in vivo* neuronal hMeDIP-seq and *in vitro* neuronal RNA-seq implicate downstream synaptic plasticity gene networks as regulators of neuronal function and cognitive processes. We anticipate these data will prompt mechanistic investigations delineating the contribution of identified genes within the observed gene networks in mediating memory enhancements observed following loss of neuronal Tet2.

ACKNOWLEDGMENTS

Work was funded by qB3 Frontiers in Medical Research fellowship (K.J.B.P), T32 DSCB Training Grant (T32 HD 007470) (K.J.B.P.), NIH Ruth L. Kirschstein NRSA fellowship (J.M.S, F32-AG055292), Irene Diamond Fund AFAR award (G.G), Simons Foundation (S.A.V), NIA (RF1 AG062357, R01 AG077770). We acknowledge the UCSF Parnassus Flow Core (RRID:SCR_018206) and support by DRC Center Grant NIH P30 DK063720 for assistance with Flow Cytometry. We thank the UCSF Center for Advanced Technology for assistance with RNA-sequencing. Some computing was performed on the Sherlock cluster. We thank Stanford University and the Stanford Research Computing Center for providing computational resources and support.

Materials and Methods

RESOURCE AVAILABILITY

Lead contact. Further information and requests for resources and reagents should be directed to and will be fulfilled by the lead contact, Dr. Saul Villeda (saul.villeda@ucsf.edu).

Materials Availability. Plasmids generated in this study are available upon request.

Data and Code Availability.

- All RNA-Seq and hMeDIP-Seq data have been deposited in the Gene Expression Omnibus and are publicly available as of the date of publication. Accession numbers are listed in the key resources table.
- This paper does not report original code.
- Any additional information required to reanalyze the data reported in this paper is available from the Lead Contact upon request.

EXPERIMENTAL MODEL AND SUBJECT DETAILS

Animal models. The following mouse lines were used: C57BL/6J (The Jackson Laboratory; stock number: 000664), *Tet2*^{flox/flox} (The Jackson Laboratory; stock number: 017573) mice, and *CamKIIa-CreER*^{T2} mice (The Jackson Laboratory; stock number: 012362). All mice used were on a C57BL/6 genetic background. Mice carrying a *Tet2*^{flox/flox} gene were crossed with mice carrying an inducible *CamKIIa-Cre-ER*^{T2} gene to obtain *Tet2*^{flox/flox}/*CamKIIa-CreER*^{T2+/0} mice. All studies were done in male mice. Studies were performed in mice starting at 3-4 months of age with *Tet2*^{flox/flox}/*CamKIIa-CreER*^{T2+/0} behavioral testing performed at 8 months of age. Animals were individually housed after stereotaxic injections or tamoxifen injections for the duration of

behavioral testing. The numbers of mice used to result in statistically significant differences was calculated using standard power calculations with $\alpha = 0.05$ and a power of 0.8. We used an online tool (<http://www.stat.uiowa.edu/~rlenth/Power/index.html>) to calculate power and sample size on the basis of experience with the respective tests, variability of the assays and inter- individual differences within groups. Mice were housed under specific pathogen-free conditions under a 12-h light- dark cycle and all animal handling and use was in accordance with institutional guidelines approved by the University of California San Francisco Institutional Animal Care and Use Committee (IACUC).

Primary neuron cultures. Primary mouse hippocampal and cortical neurons were dissociated into single-cell suspensions from E17 mouse embryo (C57Bl/6J) brains with a papain dissociation system (Worthington, Cat# LK003153). Neurons were seeded onto poly-L-lysine (Sigma Aldrich, Cat# P6282) coated plates [0.1% (wt/vol)] and grown in Neurobasal medium (Thermo Fisher, Cat# 21103049) supplemented with B-27 serum-free supplement (Thermo Fisher, Cat# 17504044), GlutaMAX (Thermo Fisher, Cat# 35050061) and penicillin–streptomycin (Thermo Fisher, Cat# 15140122) in a humidified incubator at 37 °C, with 5% CO₂. Half-media changes were performed every 4–5 days. Neurons were plated on 12 mm glass coverslips (Carolina Biological Supplies cat# 633009) in 24-well plates (100,000 cells/well) and in 12-well plates for molecular studies (500,000 cells/well). Neurons were infected with lentivirus on day 8 in vitro (DIV 8), and processed for further analyses on DIV11 for RNA analysis and DIV14 for immunohistochemical analysis. For immunocytochemistry, cells were fixed for 10 minutes with 4% paraformaldehyde, then washed and stained with MAP2 antibody (Sigma-Aldrich, Cat# M1406, RRID:AB_477171), turbo-GFP antibody (Thermo Fisher, Cat# PA5-22688, RRID:AB_2540616) to confirm lentiviral infection, and Hoechst 33342 (Thermo Fisher, Cat# H3570). Cells were lysed in Buffer RLT (Qiagen, Cat# 74004) for downstream RNA isolation.

METHOD DETAILS

RNAScope. In situ hybridization experiments and fluorescent immunostainings were performed using the RNAScope Multiplex Fluorescent Reagent Kit V2 and the RNA-Protein Co-Detection Ancillary Kit (ACD Bio, Cat# 323100 and 323180). The manufacturer recommended workflow for RNAScope with immunofluorescence co-detection was adapted for free-floating fixed-frozen sections. Briefly, cryo-preserved 40 μm thick coronal brain sections were washed in PBS and pre-treated in 200ul hydrogen peroxide provided in the RNAScope Reagent kit. Antigen retrieval was performed in 1x co-detection target retrieval buffer for 10 min at 95°C. Sections were washed two times in PBS before incubation with the primary antibodies (NeuN (Millipore Cat# MAB377, RRID:AB_2298772), Iba1 (FUJIFILM Wako Shibayagi Cat# 016-26721, RRID:AB_2811160), GFAP (Synaptic Systems Cat# 173 004, RRID:AB_10641162)) in co-detection antibody diluent overnight at 4°C. The next day, the sections were washed in PBS (Thermo Fisher, Cat# 10010023), mounted in phosphate buffer on Superfrost plus slides and air dried for 1h at room temperature. Downstream RNAScope processing followed the manufacturer's instructions. Briefly, sections were treated for 10 min with RNAScope Protease III, incubated for 2 hours with the Tet2 RNAScope probe (ACD Bio, Cat# 511591) in a HybEZ oven set at 40°C. Following amplification steps, mouse *Tet2* transcripts were detected using TSA Plus Cy3 reagents (Akoya Biosciences, Cat# SKU NEL744001KT). For immunohistochemical labeling with antibodies following the RNAScope assay, tissues were incubated with Alexa-Fluor-conjugated secondary antibodies in co-detection antibody diluent immediately after developing the HRP-TSA Plus signal. Sections were placed on a coverslip using Prolong Diamond and stored at 4°C. All slides were imaged within two weeks using a Zeiss LSM 800 confocal microscope with 20x and 63x objectives. For quantifications, stacks of 1 μm thick slices were acquired of the dentate gyrus in the hippocampus. Number of puncta per cell (neurons, microglia, astrocytes with clearly

identifiable DAPI-positive nuclei) were counted and averaged for 20-40 cells from 3 sections per animal.

Viral Plasmids and Viruses. Lentiviruses (LVs) encoding shRNAs targeting endogenous mouse Tet2 were generated using the lentiviral pGreenPuro shRNA expression system (System Biosciences, Cat# SI505A-1) according to the manufacturer's instructions. The following Tet2 targeted sequences were used (Tet2-SH-C, 5'-GAATGTAACCTTGATTGTTAT-3'; Tet2 SH-D, 5'-ACCACACTCGATGCGGTATTTTC-3'). A virus encoding a shRNA targeting luciferase (SH-Luc, 5'-GCCATTCTATCCTCTAGAGGA-3') was used as a control. The lentiviral murine Tet2 overexpression construct was generated in a two-step cloning process. First, the Tet2 coding sequence (CDS) and part of the 5' and 3' untranslated regions (UTRs) was amplified from adult mouse hippocampal cDNA and cloned into the pENTR-D-TOPO vector (Thermo Fischer, cat# K240020). After sequence validation, the CDS was further PCR amplified and restriction enzyme sites (NheI and AscI) were incorporated into the forward and reverse primers. Tet2 was then ligated into a Synapsin promoter-based lentiviral plasmid using traditional restriction enzyme-based cloning strategy. A Synapsin-GFP construct based on the same lentiviral plasmid backbone was used as a control. All plasmids were validated by Sanger sequencing prior to virus production. LV particles were generated as previously described (Lin et al., 2021) with viral titers between 1.2×10^9 to 1.5×10^9 viral particles per mL. Knock-down and overexpression of Tet2 was validated by qRT-PCR.

Lentiviruses production. 293T cells were lipotransfected with 4:3:1 μg of lentiviral vector:psPax2:pCMV-VSVG (psPAX2 was a gift from Didier Trono (Addgene plasmid # 12260); pCMV-VSV-G was a gift from Bob Weinberg (Addgene plasmid # 8454, RRID:Addgene_8454)(Stewart et al., 2003). After 48 hours lentivirus-containing media was centrifuged for 5 minutes at 1000g and filtered through 45 μm filter to remove cellular debris. Media

underwent ultracentrifugation (24000 RPM for 1.5 hours) to concentrate virus. Viral pellets were gently resuspended in PBS. Lentiviral titers were between 1.2×10^9 to 1.5×10^9 viral particles per mL. Primary neuron cell cultures were infected at an ROI of 1, and viral solutions were diluted to 1.0×10^8 viral particles/mL prior to *in vivo* stereotaxic injection.

RNA extraction, cDNA synthesis and qPCR. Total RNA was isolated using phenol/chloroform extraction according to manufacturer's protocols combined with columns from the RNeasy kit (QIAGEN, Cat# 74104). To quantify mRNA expression levels, equal amounts of cDNA were synthesized using the High-Capacity cDNA Reverse Transcription kit (ThermoFisher, Cat# 4374966) and mixed with the KAPA SYBR Fast mix (Roche, Cat# KK4601), and primers. GAPDH mRNA was amplified as an internal control. Quantitative RT-PCR was carried out in a CFX384 Real Time System (Bio-Rad).

Primer Set	Forward Primer	Reverse Primer
Gapdh	AACAGCAACTCCCACTCTTC	CCTGTTGCTGTAGCCGTATT
Tet1	GAAGCTGCACCCTGTGAG	GACAGCAGCCACACTTGGTC
Tet2	AGTAGGACTGAGAAGGGAAAGT	CGGTTGTGCTGTCATTTGTTT
Tet3	TCACAGCCTGCATGGACTTC	ACGCAGCGATTGTCTTCCTT

Library generation and RNA sequencing. After RNA isolation, RNA- sequencing libraries were constructed using the Smart-Seq2 protocol from (Picelli et al., 2014), with modifications. Briefly, 8 ng of high-quality RNA was reverse transcribed using SuperScript II (Life Technologies, Cat# 18064-014) with a poly-dT anchored oligonucleotide primer, and a template switching oligonucleotide (TSO) primer that generated homotypic PCR primer binding sites. The cDNA underwent 10 rounds of PCR amplification using KAPA HiFi Hotstart (Kapa Biosystems, Cat# KK2601), followed by Ampure bead (Beckman Coulter, Cat# A63881) clean-up. The quality of the amplified cDNA was tested using Qubit nucleic acid quantitation (Life Technologies). 2ng of high-

quality amplified cDNA was fragmented with the Tn5 transposase from the Illumina Nextera kit (Illumina, Cat# FC-131-1096) to a median size of ~500 bp. The fragmented libraries were amplified with indexed Nextera primers (Illumina, Cat# FC-131-1002) using 12 rounds of PCR. Final libraries were purified with AMPure beads and quantified on an Agilent Bioanalyzer. Libraries were pooled for sequencing on an Illumina NovaSeq with an SP flow cell (paired reads 2 × 150 bp).

RNA-Sequencing Analysis. Alignment of RNA-sequencing reads to the mouse mm10 transcriptome was performed using STAR v2.7.3a (Dobin et al., 2013) following ENCODE standard options, read counts were generated using RSEM v1.3.1 (Li and Dewey, 2011), and differential expression analysis was performed in R v4.0.2 using the DESeq2 v1.28.1 (Love et al., 2014) (detailed pipeline v2.1.2 and options available on <https://github.com/emc2cube/Bioinformatics/>). All data available under Gene Expression Omnibus accession no. GSE171295 (Token code: ehunomscxdedtkz). The derived differential gene expression lists underwent gene ontology analysis using Panther.

Stereotaxic injections. Stereotaxic injections were performed according to the protocol previously described (Lin et al., 2021). Animals were placed in a stereotaxic frame and anesthetized with 2% isoflurane (Patterson Veterinary) (2 L per min oxygen flow rate) delivered through an anesthesia nose cone. Fur around the incision area was trimmed and ophthalmic eye ointment was applied to the cornea to prevent desiccation during surgery. Viral solutions were injected bilaterally into the hippocampal CA1 and dentate gyrus regions using the following coordinates: (from bregma) anterior = -2 mm, lateral = 1.5 mm and (from skull surface) height = -1.7 and -2.1 mm. A 2 µL volume of viral solution was injected stereotaxically over 10 min (injection speed: 0.20 µL per min) using a 5-µL 26s-gauge Hamilton syringe into each locale. To limit reflux along the injection track, the needle was maintained *in situ* for 8 min, slowly pulled out half-way and kept in position for an

additional 2 min. The skin was closed using silk suture and VetBond glue. Each mouse was injected subcutaneously with saline, enrofloxacin (Bayer) antibiotic, carprofen (Patterson), and buprenorphine (Butler Schein) as directed for pain, single-housed, and monitored during recovery.

Tamoxifen administration. All experimental genetic mouse models (*Tet2^{flox/flox}* control and *Tet2^{flox/flox}/CamKIIa-CreER^{T2+/0}* mutant mice) received tamoxifen. At 4 months mice were administered tamoxifen to induce *Tet2* excision specifically in mature forebrain excitatory (adult glutamatergic) neurons termed Neuron *Tet2 cKO*. Tamoxifen (Sigma-Aldrich, Cat# T5648) was dissolved in sunflower seed oil/ethanol (10:1) at 30 mg/ml and administered intraperitoneally at 180 mg/kg body weight once per day for 5 days.

Neuronal nuclei isolation. Neuronal nuclei were isolated based on the protocol previously described with minor modifications (Krishnaswami et al., 2016). Briefly, flash-frozen dissected hippocampi were dounce homogenized (Wheaton, Cat# 357538) in 750 μ l of Homogenization buffer (HB: 250 mM sucrose, 25mM KCl, 5 mM MgCl₂, 10mM Tris pH = 8.0, 1 μ M DTT, 0.1% v/v Triton X-100, 1x RNAse Inhibitor, 1x protease inhibitor, Nuclease-free H₂O) with 12 strokes of the loose pestle and 20 strokes of the tight pestle. Samples were filtered through a 40 μ m filter and centrifuged at 500 RCF for 6 min at 4 °C. Samples were resuspended in 750 μ l HB and spun at 500 RCF for 8 min at 4 °C. Samples were incubated for 15 minutes on ice in staining buffer (0.5% wt/vol BSA in PBS). Conjugated mouse monoclonal anti-NeuN-AlexaFluor488 antibody (Millipore, Cat# MAB377X, RRID:AB_2149209) was added to the tube at a final dilution of 1:250. Samples were incubated on a tube rotator for 60 min at 4 °C and then spun for 5 min at 500g at 4 °C. Samples were washed 2x with 1000 μ l staining buffer and Hoechst 44432 was added to staining buffer at a final concentration of 0.01 μ g/ml. Samples were then filtered through a 35 μ m FACS tube filter and sorted.

Fluorescence activated cell sorting (FACS). Nuclei were sorted on a BD FACSAria Fusion with a 70 µm nozzle and with a flow rate of 1-2.5. Nuclei were first gated by forward and side scatter, then gated for doublets with height and width. Nuclei that were both Hoechst+ and NeuN+ were sorted into Tri Reagent (Sigma Aldrich, T9424) for RNA analysis or PBS for DNA analysis.

hMeDIP-Seq Library Preparation. For each library, 200ng of DNA was sonicated to 300-500 base pairs, and after end cleanup and A-tailing (End-It DNA End-Repair Kit, Lucigen, Cat# ER0720), NEBNext adapters were ligated onto the samples (NEB Ultra DNA library kit, NEB, Cat# E7805S). Samples were then divided into input and immunoprecipitation samples. DNA was denatured by heating at 95°C for 10 minutes, followed by plunging the samples on ice. Ice-cold 10x hMeDIP buffer (100mM NaPO₄ pH 7.0, 1.4 mM NaCl, and 0.5% Triton X-100) was added to the immunoprecipitation sample to a final concentration of 1x. 0.2 µL of 5hmC DNA antibody (Active Motif, Cat# 39769, RRID:AB_10013602) was added to the samples. The samples were rotated overnight at 4 °C. Protein A magnetic beads (NEB, Cat# S1425S) were added to the reaction, and rotated at 4°C for 2 hours. The samples were collected on a magnetic rack, and the samples were washed three times (with 10 minutes incubations) with ice cold 1x hMeDIP buffer. DNA was eluted from the beads by shaking the samples in lysis buffer (50mM Tris pH 8.0, 10mM EDTA, and 0.5% SDS) with proteinase K (100 µg/ml, Sigma Aldrich, Cat# 03115879001) at 55°C for 3+ hours. The DNA was purified by phenol/chloroform extraction followed by ethanol precipitation. After purification, the libraries were PCR amplified (KAPA HiFi, kk2602) for 14 cycles using paired-end indexed primers (NEBNext Multiplex Oligos (Set 1), NEB, Cat# E7335L). Libraries were pooled and purified with 1.8X Agencourt AMPure XP beads (Beckman Coulter, A63881). Individual libraries were quantified on the Agilent Bioanalyzer with the DNA sensitivity protocol and pooled for sequencing.

hMeDIP-Seq Analysis. hMeDIP-Seq libraries were sequenced on the Illumina HiSeq4000 to a average depth of over 50 million reads. Fastq files were uploaded to Galaxy (usegalaxy.org) for mapping using Bowtie 2 and peak finding with MACS2 (Afgan et al., 2018; Feng et al., 2012; Langmead and Salzberg, 2012). Libraries were mapped to the mm10 genome using Bowtie 2 with default parameters. MACS2 was used to determine peaks that were lost after overexpression of Tet2 or deletion of Tet2 with the following change to default parameters: minimum enrichment changed to 2-fold. Peaks were associated with genes if they overlapped or were the closest gene (by transcriptional start site) to the peak. The derived gene list underwent gene ontology analysis using Panther. All data available under Gene Expression Omnibus accession no. GSE198910 (Token code: uvmzaumuxneljsd) and GSE199597 (Token code: cvytgeejqpybzwr).

Open Field. Mice were placed in the center of an open 40cm x 40cm square chamber (Kinder Scientific) with no cues or stimuli and allowed to move freely for 10 minutes. Infrared photobeam breaks were recorded and movement metrics analyzed by MotorMonitor software (Kinder Scientific).

Novel Object Recognition. The novel object recognition task was preformed according to the protocol previously described (White et al., 2020). During the habituation phase (day 1), mice could freely explore an empty arena for 10 minutes. During the training phase (day 2), two identical objects were placed in the habituated arena, and mice could explore the objects for 5 minutes. For the testing phase (day 3), one object was replaced with a novel object, and mice could explore the objects for 5 minutes. Time spent exploring each object was quantified using the Smart Video Tracking Software (Panlab; Harvard Apparatus). Two different sets of objects are used. To control for any inherent object preference, half of the mice are exposed to object A as their novel object and half to object B. To control for any potential object-independent location preference, the location of the novel object relative to the trained object is also varied. The objects were chosen based on their ability to capture the animal's interest, independent of genetic

background or age. To determine percent time with novel object, we calculate $(\text{Time with novel object}) / (\text{Time with Trained Object} + \text{Time with Novel Object}) * 100$. In this preference index, 100% indicates full preference for the novel object, and 0% indicates full preference for the trained object. A mouse with a value of 50% would have spent equal time exploring both objects. Mice that did not explore both objects during the training phase were excluded from analysis.

Radial arm water maze. Spatial learning and memory was assessed using the radial arm water maze (RAWM) paradigm according to the protocol previously described (Alamed et al., 2006). In this task the goal arm location containing a platform remains constant throughout the training and testing phase, while the start arm is changed during each trial. Spatial cues are posted on all four walls of the RAWM area. Entry into an incorrect arm is scored as an error, and errors are averaged over training blocks (three consecutive trials). On day one, during the training phase, mice are trained for 15 trials, with trials alternating between a visible and hidden platform for blocks 1-4 and then switching to only a hidden platform in block 5. On day 2 during the testing phase, mice are tested for 15 trials with a hidden platform for blocks 6-10. Investigators were blinded to genotype and treatment when scoring.

Fear conditioning. In this task, mice learned to associate the environmental context (fear conditioning chamber) with an aversive stimulus (mild foot shock; unconditioned stimulus, US) enabling testing for hippocampal-dependent contextual fear conditioning. To also assess amygdala-dependent cued fear conditioning, the mild foot shock was paired with a light and tone cue (conditioned stimulus, CS). Conditioned fear was displayed as freezing behavior. Specific training parameters are as follows: tone duration is 30 seconds; level is 70 dB, 2 kHz; shock duration is 2 seconds; intensity is 0.6 mA. This intensity is not painful and can easily be tolerated but will generate an unpleasant feeling. On day one, each mouse was placed in a fear-conditioning chamber and allowed to explore for two minutes before delivery of a 30-second tone (70 dB) ending with a 2-second foot shock (0.6 mA). Two minutes later, a second CS-US pair was

delivered. On day 2, each mouse was first placed in the fear-conditioning chamber containing the same exact context, but with no CS or foot shock. Freezing was analyzed for 2 minutes. One hour later, the mice were placed in a new context containing a different odor, cleaning solution, floor texture, chamber walls and shape. Animals were allowed to explore for 2 minutes before being re-exposed to the CS. Freezing was analyzed for 3 minutes using a FreezeScan video tracking system and software (Cleversys, Inc).

QUANTIFICATION AND STATISTICAL ANALYSIS

Data and statistical analysis. Graphed data are expressed as mean \pm SEM. Statistical analysis was performed with Prism 8.0 software (GraphPad Software). Unless otherwise noted, means between two groups were compared with two-tailed, unpaired Student's t-test. Comparisons of means from multiple groups with each other or against one control group were analyzed with one-way ANOVA and Tukey's post-hoc test. All histology and behavior experiments conducted were done in a randomized and blinded fashion. For each experiment, the overall size of the experimental groups corresponded to distinct animals or cultures. Unique samples were not measured repeatedly within the same characterization of a given cohort.

REFERENCES

Afgan, E., Jalili, V., Goonasekera, N., Taylor, J., and Goecks, J. (2018). Federated Galaxy: Biomedical Computing at the Frontier. *Proc. IEEE Int. Conf. Cloud Comput. 2018*.

<https://doi.org/10.1109/cloud.2018.00124>.

Alamed, J., Wilcock, D.M., Diamond, D.M., Gordon, M.N., and Morgan, D. (2006). Two-day radial-arm water maze learning and memory task; robust resolution of amyloid-related memory deficits in transgenic mice. *Nat. Protoc. 1*, 1671–1679. <https://doi.org/10.1038/nprot.2006.275>.

Carrillo-Jimenez, A., Deniz, Ö., Niklison-Chirou, M.V., Ruiz, R., Bezerra-Salomão, K., Stratoulis, V., Amouroux, R., Yip, P.K., Vilalta, A., Cheray, M., et al. (2019). TET2 Regulates the Neuroinflammatory Response in Microglia. *Cell Rep. 29*, 697-713.e8. <https://doi.org/10.1016/j.celrep.2019.09.013>.

Chouliaras, L., van den Hove, D.L.A., Kenis, G., Keitel, S., Hof, P.R., van Os, J., Steinbusch, H.W.M., Schmitz, C., and Rutten, B.P.F. (2012). Age-related increase in levels of 5-hydroxymethylcytosine in mouse hippocampus is prevented by caloric restriction. *Curr. Alzheimer Res. 9*, 536–544. <https://doi.org/10.2174/156720512800618035>.

Dobin, A., Davis, C.A., Schlesinger, F., Drenkow, J., Zaleski, C., Jha, S., Batut, P., Chaisson, M., and Gingeras, T.R. (2013). STAR: ultrafast universal RNA-seq aligner. *Bioinforma. Oxf. Engl. 29*, 15–21. <https://doi.org/10.1093/bioinformatics/bts635>.

Dong, E., Gavin, D.P., Chen, Y., and Davis, J. (2012). Upregulation of TET1 and downregulation of APOBEC3A and APOBEC3C in the parietal cortex of psychotic patients. *Transl. Psychiatry* 2, e159. <https://doi.org/10.1038/tp.2012.86>.

Feng, J., Zhou, Y., Campbell, S.L., Le, T., Li, E., Sweatt, J.D., Silva, A.J., and Fan, G. (2010). Dnmt1 and Dnmt3a maintain DNA methylation and regulate synaptic function in adult forebrain neurons. *Nat. Neurosci.* 13, 423–430. <https://doi.org/10.1038/nn.2514>.

Globisch, D., Münzel, M., Müller, M., Michalakis, S., Wagner, M., Koch, S., Brückl, T., Biel, M., and Carell, T. (2010). Tissue distribution of 5-hydroxymethylcytosine and search for active demethylation intermediates. *PLoS One* 5, e15367. <https://doi.org/10.1371/journal.pone.0015367>.

Gontier, G., Iyer, M., Shea, J.M., Bieri, G., Wheatley, E.G., Ramalho-Santos, M., and Villeda, S.A. (2018). Tet2 Rescues Age-Related Regenerative Decline and Enhances Cognitive Function in the Adult Mouse Brain. *Cell Rep.* 22, 1974–1981. <https://doi.org/10.1016/j.celrep.2018.02.001>.

Gulmez Karaca, K., Kupke, J., Brito, D.V.C., Zeuch, B., Thome, C., Weichenhan, D., Lutsik, P., Plass, C., and Oliveira, A.M.M. (2020). Neuronal ensemble-specific DNA methylation strengthens engram stability. *Nat. Commun.* 11, 639. <https://doi.org/10.1038/s41467-020-14498-4>.

Guo, J.U., Ma, D.K., Mo, H., Ball, M.P., Jang, M.-H., Bonaguidi, M.A., Balazer, J.A., Eaves, H.L., Xie, B., Ford, E., et al. (2011). Neuronal activity modifies the DNA methylation landscape in the adult brain. *Nat. Neurosci.* 14, 1345–1351. <https://doi.org/10.1038/nn.2900>.

Hwang, J.-Y., Aromolaran, K.A., and Zukin, R.S. (2017). The emerging field of epigenetics in neurodegeneration and neuroprotection. *Nat. Rev. Neurosci.* *18*, 347–361. <https://doi.org/10.1038/nrn.2017.46>.

Ito, S., Shen, L., Dai, Q., Wu, S.C., Collins, L.B., Swenberg, J.A., He, C., and Zhang, Y. (2011). Tet proteins can convert 5-methylcytosine to 5-formylcytosine and 5-carboxylcytosine. *Science* *333*, 1300–1303. <https://doi.org/10.1126/science.1210597>.

Jaenisch, R., and Bird, A. (2003). Epigenetic regulation of gene expression: how the genome integrates intrinsic and environmental signals. *Nat. Genet.* *33 Suppl*, 245–254. <https://doi.org/10.1038/ng1089>.

Kaas, G.A., Zhong, C., Eason, D.E., Ross, D.L., Vachhani, R.V., Ming, G.-L., King, J.R., Song, H., and Sweatt, J.D. (2013). TET1 controls CNS 5-methylcytosine hydroxylation, active DNA demethylation, gene transcription, and memory formation. *Neuron* *79*, 1086–1093. <https://doi.org/10.1016/j.neuron.2013.08.032>.

Khare, T., Pai, S., Koncevicius, K., Pal, M., Kriukiene, E., Liutkeviciute, Z., Irimia, M., Jia, P., Ptak, C., Xia, M., et al. (2012). 5-hmC in the brain is abundant in synaptic genes and shows differences at the exon-intron boundary. *Nat. Struct. Mol. Biol.* *19*, 1037–1043. <https://doi.org/10.1038/nsmb.2372>.

Koopmans, F., van Nierop, P., Andres-Alonso, M., Byrnes, A., Cijssouw, T., Coba, M.P., Cornelisse, L.N., Farrell, R.J., Goldschmidt, H.L., Howrigan, D.P., et al. (2019). SynGO: An Evidence-Based, Expert-Curated Knowledge Base for the Synapse. *Neuron* 103, 217-234.e4. <https://doi.org/10.1016/j.neuron.2019.05.002>.

Kriaucionis, S., and Heintz, N. (2009). The nuclear DNA base 5-hydroxymethylcytosine is present in Purkinje neurons and the brain. *Science* 324, 929–930. <https://doi.org/10.1126/science.1169786>.

Krishnaswami, S.R., Grindberg, R.V., Novotny, M., Venepally, P., Lacar, B., Bhutani, K., Linker, S.B., Pham, S., Erwin, J.A., Miller, J.A., et al. (2016). Using single nuclei for RNA-seq to capture the transcriptome of postmortem neurons. *Nat. Protoc.* 11, 499–524. <https://doi.org/10.1038/nprot.2016.015>.

Li, X., Yao, B., Chen, L., Kang, Y., Li, Y., Cheng, Y., Li, L., Lin, L., Wang, Z., Wang, M., et al. (2017). Ten-eleven translocation 2 interacts with forkhead box O3 and regulates adult neurogenesis. *Nat. Commun.* 8, 15903. <https://doi.org/10.1038/ncomms15903>.

Lin, K., Bieri, G., Gontier, G., Müller, S., Smith, L.K., Snethlage, C.E., White, C.W., Maybury-Lewis, S.Y., and Villeda, S.A. (2021). MHC class I H2-Kb negatively regulates neural progenitor cell proliferation by inhibiting FGFR signaling. *PLoS Biol.* 19, e3001311. <https://doi.org/10.1371/journal.pbio.3001311>.

Liu, C., Sun, X., Wang, Z., Le, Q., Liu, P., Jiang, C., Wang, F., and Ma, L. (2018). Retrieval-Induced Upregulation of Tet3 in Pyramidal Neurons of the Dorsal Hippocampus Mediates Cocaine-Associated Memory Reconsolidation. *Int. J. Neuropsychopharmacol.* 21, 255–266. <https://doi.org/10.1093/ijnp/pyx099>.

Love, M.I., Huber, W., and Anders, S. (2014). Moderated estimation of fold change and dispersion for RNA-seq data with DESeq2. *Genome Biol.* 15, 550. <https://doi.org/10.1186/s13059-014-0550-8>.

Marshall, L.L., Killinger, B.A., Ensink, E., Li, P., Li, K.X., Cui, W., Lubben, N., Weiland, M., Wang, X., Gordevicius, J., et al. (2020). Epigenomic analysis of Parkinson's disease neurons identifies Tet2 loss as neuroprotective. *Nat. Neurosci.* 23, 1203–1214. <https://doi.org/10.1038/s41593-020-0690-y>.

Miller, C.A., and Sweatt, J.D. (2007). Covalent modification of DNA regulates memory formation. *Neuron* 53, 857–869. <https://doi.org/10.1016/j.neuron.2007.02.022>.

Moore, L.D., Le, T., and Fan, G. (2013). DNA methylation and its basic function. *Neuropsychopharmacol. Off. Publ. Am. Coll. Neuropsychopharmacol.* 38, 23–38. <https://doi.org/10.1038/npp.2012.112>.

Picelli, S., Faridani, O.R., Björklund, A.K., Winberg, G., Sagasser, S., and Sandberg, R. (2014). Full-length RNA-seq from single cells using Smart-seq2. *Nat. Protoc.* 9, 171–181. <https://doi.org/10.1038/nprot.2014.006>.

Rasmussen, K.D., and Helin, K. (2016). Role of TET enzymes in DNA methylation, development, and cancer. *Genes Dev.* *30*, 733–750. <https://doi.org/10.1101/gad.276568.115>.

Rudenko, A., Dawlaty, M.M., Seo, J., Cheng, A.W., Meng, J., Le, T., Faull, K.F., Jaenisch, R., and Tsai, L.-H. (2013). Tet1 is critical for neuronal activity-regulated gene expression and memory extinction. *Neuron* *79*, 1109–1122. <https://doi.org/10.1016/j.neuron.2013.08.003>.

Stewart, S.A., Dykxhoorn, D.M., Palliser, D., Mizuno, H., Yu, E.Y., An, D.S., Sabatini, D.M., Chen, I.S.Y., Hahn, W.C., Sharp, P.A., et al. (2003). Lentivirus-delivered stable gene silencing by RNAi in primary cells. *RNA N. Y. N* *9*, 493–501. <https://doi.org/10.1261/rna.2192803>.

Szulwach, K.E., Li, X., Li, Y., Song, C.-X., Wu, H., Dai, Q., Irier, H., Upadhyay, A.K., Gearing, M., Levey, A.I., et al. (2011). 5-hmC-mediated epigenetic dynamics during postnatal neurodevelopment and aging. *Nat. Neurosci.* *14*, 1607–1616. <https://doi.org/10.1038/nn.2959>.

Tahiliani, M., Koh, K.P., Shen, Y., Pastor, W.A., Bandukwala, H., Brudno, Y., Agarwal, S., Iyer, L.M., Liu, D.R., Aravind, L., et al. (2009). Conversion of 5-methylcytosine to 5-hydroxymethylcytosine in mammalian DNA by MLL partner TET1. *Science* *324*, 930–935. <https://doi.org/10.1126/science.1170116>.

White, C.W., Fan, X., Maynard, J.C., Wheatley, E.G., Bieri, G., Couthouis, J., Burlingame, A.L., and Villeda, S.A. (2020). Age-related loss of neural stem cell O-GlcNAc promotes a glial fate switch through STAT3 activation. *Proc. Natl. Acad. Sci. U. S. A.* *117*, 22214–22224. <https://doi.org/10.1073/pnas.2007439117>.

Yu, H., Su, Y., Shin, J., Zhong, C., Guo, J.U., Weng, Y.-L., Gao, F., Geschwind, D.H., Coppola, G., Ming, G., et al. (2015). Tet3 regulates synaptic transmission and homeostatic plasticity via DNA oxidation and repair. *Nat. Neurosci.* *18*, 836–843. <https://doi.org/10.1038/nn.4008>.

Publishing Agreement

It is the policy of the University to encourage open access and broad distribution of all theses, dissertations, and manuscripts. The Graduate Division will facilitate the distribution of UCSF theses, dissertations, and manuscripts to the UCSF Library for open access and distribution. UCSF will make such theses, dissertations, and manuscripts accessible to the public and will take reasonable steps to preserve these works in perpetuity.

I hereby grant the non-exclusive, perpetual right to The Regents of the University of California to reproduce, publicly display, distribute, preserve, and publish copies of my thesis, dissertation, or manuscript in any form or media, now existing or later derived, including access online for teaching, research, and public service purposes.

DocuSigned by:

Karishma Pratt

5F2275195D0D4F2...

Author Signature

8/30/2023

Date